J. Fluid Mech. (2011), *vol.* 666, *pp.* 273–307.
doi:10.1017/S0022112010004180

Fluid flows driven by light scattering

R. WUNENBURGER†, B. ISSENMANN, E. BRASSELET, C. LOUSSERT, V. HOURTANE AND J.-P. DELVILLE

Centre de Physique Moléculaire Optique et Hertzienne, UMR CNRS 5798, Université Bordeaux I, 351 cours de la Libération, 33405 Talence CEDEX, France

(Received 20 May 2009; revised 28 July 2010; accepted 3 August 2010; first published online 15 November 2010)

We report on the direct experimental observation of laser-induced flows in isotropic liquids that scatter light. We use a droplet microemulsion in the two-phase regime, which behaves like a binary mixture. Close to its critical consolute line, the microemulsion undergoes large refractive index fluctuations that scatter light. The radiation pressure of a laser beam is focused onto the soft interface between the two phases of the microemulsion and induces a cylindrical liquid jet that continuously emits droplets. We demonstrate that this dripping phenomenon takes place as a consequence of a steady flow induced by the transfer of linear momentum from the optical field to the liquid due to light scattering. We first show that the cylindrical jet guides light as a step-index liquid optical fiber whose core diameter is self-adapted to the light itself. Then, by modelling the light-induced flow as a low-Reynolds-number, parallel flow, we predict the dependence of the dripping flow rate on the thermophysical properties of the microemulsion and the laser beam power. Satisfying agreement is found between the model and experiments.

Key words: electrohydrodynamic effects, interfacial flows (free surface), MEMS/NEMS

1. Introduction

Liquid manipulation by external fields (e.g. electric or magnetic) have been much more studied using static fields rather than propagating fields such as those associated with electromagnetic or acoustic waves (Eggers & Villermaux 2008). This may be explained by the complexity of these phenomena whose description combines wave physics with hydrodynamics. Although liquid flows and interface deformations induced by propagating fields have some similarities to those induced by static fields, they exhibit unique features associated with the very nature of wave propagation and to the feedback on the wave propagation itself (Casner & Delville 2003, 2004; Casner, Delville & Brevik 2003; Schroll *et al.* 2007; Brasselet, Wunenburger & Delville 2008).

The present work focuses on the bulk flow induced by a laser beam within a liquid that scatters light. More precisely, we analyse both experimentally and theoretically the steady flow established within light-induced liquid jets (an example is shown in figure 1*a*). Such jets are obtained by destabilizing the interface of a near-critical liquid binary mixture in the two-phase regime using the radiation pressure of a vertical laser beam impinging on the liquid interface, as sketched in figure 1(*b*). In addition, a continuous droplet emission is observed at their tip, as illustrated in figure 1(*a*).

† Email address for correspondence: r.wunenburger@cpmoh.u-bordeaux1.fr

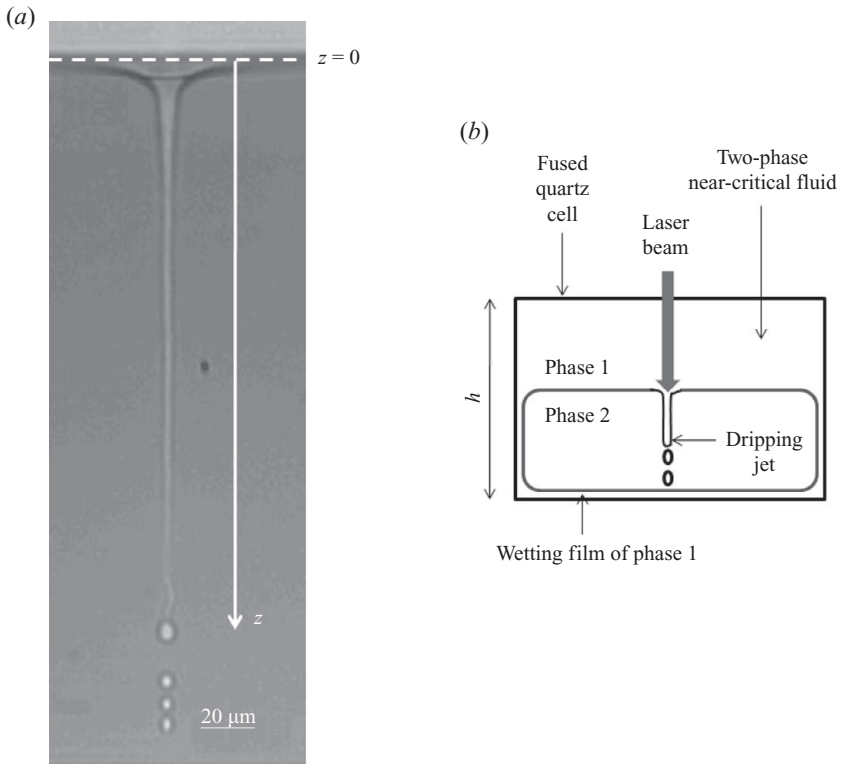

FIGURE 1. (*a*) Picture of the liquid jet obtained when the interface of a near-critical liquid binary mixture in the two-phase regime is destabilized by the radiation pressure of a laser beam impinging on the interface from above, i.e. from the liquid phase of largest refractive index in our case. The steady-state dripping jet demonstrates that a steady flow is established within the jet (beam waist $w_0 = 3.47\,\mu\text{m}$, beam power $\mathscr{P} = 378\,\text{mW}$, sample temperature T such that $T - T_c = \Delta T = 4\,\text{K}$, T_c being the critical temperature of the binary mixture). (*b*) Sketch of the experiment.

We will show that this flow results from the bulk force exerted by the light scattered by the refractive index inhomogeneities of the near-critical fluid, hereafter called the scattering force density, $\boldsymbol{f}^{scatt}$. A jet turns out to be the result of a complex interplay between the radiation pressure that is a surface stress exerted perpendicular to the liquid–liquid interface and the scattering force density that is parallel to the laser beam. Here we aim at explaining why and how liquid flows inside the jet, whereas the understanding of the jet length and its dripping mechanism are beyond the scope of our study.

We notice that the usual dependence of the flow rate Q within a tube of axis (Oz) having solid or liquid walls on the externally imposed force density $\mathrm{d}p/\mathrm{d}z$ is the linear Poiseuille law $Q \propto \mathrm{d}p/\mathrm{d}z$. Assuming that the scattering force density $f^{scatt} \propto \mathscr{P}$ plays the role of a pressure gradient $\mathrm{d}p/\mathrm{d}z$ in the light-induced flow experiment (p is the fluid pressure, $\mathscr{P}$ the laser beam power, (Oz) the axis of both the beam and the jet), one would expect $Q \propto \mathscr{P}$. Instead, we observe an intriguing nonlinear dependence of the form $Q \propto \mathscr{P}^{2.6}$ for which we propose a model that couples the beam propagation with the jet diameter. Moreover, we describe the liquid flow along the jet as a Poiseuille flow driven by the scattering force density in a soft-walled cylindrical tube of tunable diameter. From the quantitative agreement between the measured dripping flow rates

and the prediction of our model, we conclude that such a unique flow behaviour is the result of a self-adaptation of the jet diameter to the driving laser beam. Moreover, we demonstrate that the scattering force density is at the root of the observed dripping flow, which constitutes the first direct experimental proof of light-scattering-driven flow.

In the following, the framework of this study is introduced by presenting the various forces induced by electromagnetic waves, i.e. surface and bulk forces, and their associated hydrodynamic effects. Then we review the earlier studies on light-induced bulk flows and discuss various mechanisms of light-driven flow. This leads us to justify the choice of our system and to present the guideline of our study.

1.1. *Interface deformations induced by radiation pressure*

Since a photon possesses a linear momentum that depends on the refractive index of the medium through which it propagates, it can exchange momentum with matter when its propagation is perturbed (Pfeifer *et al.* 2007). As demonstrated by the pioneering experiments of Ashkin & Dziedzic (1973) and Zhang & Chang (1988), this momentum transfer underlies the radiation pressure that is exerted on the interface between two immiscible dielectric isotropic fluids of different refractive indices. As a result, deformation of the interface and associated flow take place (Ostrovskaya 1988*a*, *b*; Grigorova, Rastopov & Sukhodol'skii 1990; Casner & Delville 2001; Sakai, Mizumo & Takagi 2001). Using either the formalism of Maxwell's electromagnetic stress tensor (see Appendix B) or the detailed balance of momentum change of reflected and refracted photons at the interface using the ray optics approximation and Minkowski's expression of the linear momentum (Wunenburger, Casner & Delville 2006*a*), the associated electromagnetic surface stress is found to be normal to the interface and directed from the fluid of highest refractive index to the fluid of lowest refractive index. Such electromagnetic actuation of fluid interfaces is at the root of a recently developed versatile non-contact measurement technique of interfacial and bulk mechanical properties of simple and complex fluids (Mitani & Sakai 2002; Yoshitake *et al.* 2005, 2008).

Often, a steady liquid interface deformation due to a steady radiation pressure looks like the one obtained when two dielectric fluids are submitted to a static electric field. One can mention the following situations.

(*a*) When an initially flat dielectric interface is subjected to either a non-uniform static electric field (Schäffer *et al.* 2000; Sakai & Yamamoto 2006) or to an electromagnetic beam (Casner & Delville 2001; Wunenburger *et al.* 2006*a*), the resulting small-amplitude, steady deformations are bell-shaped.

(*b*) Sessile drops strongly stretched by the radiation pressure of light become cones (Chraïbi *et al.* 2008*b*) resembling those obtained using a uniform static electric field (Wohluter & Basaran 1992).

(*c*) Dielectric liquid bridges of aspect ratios larger than the Rayleigh–Plateau instability threshold value can be stabilized using either an axial uniform static electric field (Raco 1968; Gonzalez *et al.* 1989) or a coaxial laser beam (Casner & Delville 2004). Marr-Lyon, Thiessen & Marston (2001) showed that liquid bridge stabilization can also be achieved using the radiation pressure exerted on the bridge surface by a steady acoustic field.

(*d*) Dripping jets can result from the destabilization of an initially flat interface or spherical drop using either a static electric field (Zeleny 1914) or a laser beam when the beam impinges the interface from the fluid of lowest refractive index (Casner & Delville 2003).

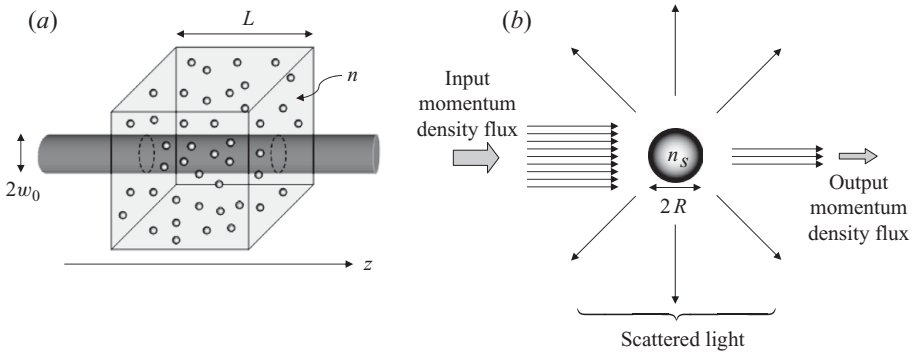

FIGURE 2. (*a*) Illustrative sketch of a light-scattering fluid sample made of a collection of individual scatterers, with refractive index n_s, that are randomly distributed in a homogeneous fluid with refractive index $n \neq n_s$. An incident laser beam of characteristic diameter $2w_0$ passes through the sample of thickness L. (*b*) Illustration of the light scattering process by a single scatterer of radius R.

However, these seemingly similar deformations are generally driven by different physical mechanisms. In case (*b*), the conical shape in the static case is due to the scale invariant divergence of the electric field, hence of the electrostatic stress, as the curvature of the deformation tip increases – a mechanism that does not hold in the propagating case. In case (*c*), optically stabilized bridges result from the guiding of light inside the liquid column (Brasselet & Delville 2008; Brasselet *et al.* 2008) – a mechanism that basically involves field propagation and the wavelength as an intrinsic length scale of the light–matter coupling, which are both irrelevant in the electrostatic case. Interestingly, we notice that large-amplitude 'nipple-like' interface deformations observed when a laser beam impinges on an interface from the fluid of lowest refractive index (Casner *et al.* 2003; Chraïbi *et al.* 2008*a*) have no equivalent under actuation by other fields. More generally, the genuine physics of interface deformations induced by electromagnetic radiation pressure is by essence due to the feedback of the deformed interface on the radiation pressure itself (Casner & Delville 2003; Wunenburger *et al.* 2006*a*; Brasselet & Delville 2008; Brasselet *et al.* 2008).

1.2. *Bulk flows induced by bulk forces*

When the radiation pressure, which acts as a normal stress (see Appendix B), is time-independent, the flow associated with the interface deformation vanishes at steady state. The shape of the interface is therefore solely determined by the balance of radiation pressure, Laplace pressure and buoyancy (Chraïbi *et al.* 2008*a*). However, steady bulk forces induced in a liquid by the scattering or the absorption of light by the medium may induce steady flows.

Savchenko, Tabiryan & Zel'dovich (1997) theoretically considered the bulk force field associated with the transfer of momentum from light to the bulk of an isotropic liquid and calculated the resulting bulk flow. To do so, either light absorbing or light scattering liquids can be used. Absorption can occur in simple fluids or in suspensions, whereas light scattering requires spatial inhomogeneities of the refractive index. A simple illustration of the latter case is depicted in figure 2(*a*). It consists of a laser beam (i.e. a flux of photons) that propagates along the z-axis through a liquid that scatters light. Such a liquid may be viewed as a collection of individual scatterers, with refractive index n_s, that are randomly distributed in a homogeneous fluid with refractive index $n \neq n_s$. The projection along z of the net momentum of the beam

thus progressively decreases during propagation due to absorption or scattering of a fraction of the incident photons, as sketched in figure 2(*b*). Consequently, a net force per unit volume, directed along z, is exerted on the bulk of the liquid: this is the scattering force density, $\boldsymbol{f}^{scatt}$.

A more detailed analysis of the light–matter interaction reveals the limited accuracy of the simple picture presented above and the associated experimental constraints. Indeed, the illumination of a homogeneous light-absorbing liquid induces heating that may give rise to thermal free convection, boiling or thermo-capillary flows when a liquid interface is present. All these effects may prevent an unambiguous observation of the bulk flow induced by the light momentum transfer. For these reasons, we shall restrict ourselves to particles suspended in non-absorbing liquids. However, we notice that although suspensions usually scatter light, they can also absorb it, thereby increasing the efficiency of the light momentum transfer. In this case, several side effects may also overcome the flow induced by the light momentum transfer, as discussed hereafter.

When aerosols are used, the differential heating of the surrounding gas by the side-illuminated particles induces a particle motion formerly called photophoresis (Rohatscheck 1985). The direction of this motion depends on the respective contributions of light refraction and absorbtion by the particle and its amplitude can be much larger than the contribution of the light momentum transfer. On the other hand, when the absorbing particles are suspended in a liquid, backward particle motion can be observed at low laser intensity (Monjushiro, Takeuchi & Watarai 2002). This results from a competition between the scattering force and still unexplained hydrodynamic effects associated with particle heating. Unexpected phenomena related to heating can be observed too at high laser intensity. For example, (i) extremely rapid particle motion (velocity of 1 μm diameter particles of order $10^4\,\mathrm{m\,s^{-1}}$) due to vaporization-induced shock waves (Zakharov, Kazaryan & Korotkov 1994) and (ii) still unexplained rapid particle motion (velocity of 2 μm diameter particles of order $10^2\,\mathrm{m\,s^{-1}}$) in either forward or backward direction depending on the light focusing (Kazaryan, Korotkov & Zakharov 1995) and that does not involve boiling. Thus, the consequences of heating due to light absorption prevent the flow due to light momentum transfer to be observed *per se*. Consequently, we will further focus our attention on non-absorbing liquid suspensions.

1.2.1. *Individual motion versus flow as a whole*

Let us consider a liquid suspension of thickness L made of non-absorbing scatterers randomly distributed in a non-absorbing liquid, as sketched in figure 2(*a*). When an incident light field is scattered by an individual scatterer, as depicted in figure 2(*b*), the spatial redistribution of the momentum of light leads to a force $\boldsymbol{F}^{scatt}$ exerted on the scatterer, which is expected to move relatively to the surrounding fluid. In general, the response of the system is described by the combination of a collective response of the suspension and a longitudinal segregation process (i.e. along the beam axis). The relative weight of these two contributions depends on the ratio $\Delta u_{\parallel}/u$, where $\Delta u_{\parallel}$ is the component of the relative velocity of the scatterers with respect to the liquid that is parallel to the beam axis and $\boldsymbol{u}$ is the average suspension velocity.

On the one hand, u is estimated from the balance between the work per unit time $\dot{\mathscr{W}}$ done by the scattering force density $\boldsymbol{f}^{scatt}$ on the liquid and the net viscous dissipation rate $\dot{\mathscr{D}}$. First, we have $\dot{\mathscr{W}} \sim f^{scatt} u w_0^2 L$, where w_0 is the characteristic beam radius and $\boldsymbol{f}^{scatt} \propto \tau \boldsymbol{S} n/c$ (the proportionality factor between $\boldsymbol{f}^{scatt}$ and $\boldsymbol{S}$ depending

on the angular distribution of the scattering of light, i.e. on the size and shape of the scatterers; see van de Hulst 1957). Here we have introduced the Poynting vector $\boldsymbol{S} = I\hat{\boldsymbol{z}}$, where I is the characteristic light beam intensity and $\hat{\boldsymbol{z}}$ is the z-axis unit vector, c is the speed of light in vacuum and $\tau = -(1/I)(\mathrm{d}I/\mathrm{d}z)$ is the intensity attenuation coefficient due to scattering (also called turbidity), which is assumed to satisfy $\tau L \ll 1$. In addition, under the assumption of low Reynolds flow, we have $\dot{\mathscr{D}} \sim L^3\eta(u/L)^2$, where η is the dynamic viscosity of the suspension. Therefore, we deduce from $\dot{\mathscr{W}} \sim \dot{\mathscr{D}}$ that $u \sim w_0^2 f^{scatt}/\eta$. On the other hand, $\Delta\boldsymbol{u}_{\parallel}$ is determined by the balance between the scattering force $\boldsymbol{F}^{scatt} = \Sigma n\boldsymbol{S}/c$ exerted on an individual scatterer (Σ is the particle scattering cross-section) and the viscous drag force $-6\pi\eta R\Delta\boldsymbol{u}_{\parallel}$, where R is the radius of the scatterers assumed to be spherical for simplicity. We thus obtain $\Delta u_{\parallel} \sim \Sigma nI/c\eta R$.

By definition, the suspension is pushed as a whole if $\Delta u_{\parallel} \ll u$. Since in the single scattering regime $\tau \sim N\Sigma$, where N is the number of scatterers per unit volume, this occurs when the volume fraction of scatterers, $\Phi = (4\pi/3)NR^3$, satisfies the condition

$$\Phi \gg \frac{R^2}{w_0^2}. \tag{1.1}$$

We notice that this constraint of small enough scatterers and/or dense enough suspensions adds to the condition of good optical transparency of the sample that is required to deal with a truly bulk force field,

$$\tau L \ll 1. \tag{1.2}$$

The above conditions may induce severe constraints on the refractive index mismatch between the scatterers and the surrounding liquid. To illustrate this, let us consider the regime of Rayleigh scattering characterized by $R \ll \lambda$ (λ is the wavelength of the light beam in the suspension). In that case, it is known that $\tau \sim NR^2(\Delta n/n)^2(kR)^4$, where $k = 2\pi/\lambda$ (van de Hulst 1957) and $\Delta n = n_s - n$, and one finds that conditions (1.1) and (1.2) are compatible only if $(\Delta n)^2(R^2/w_0^2)(L/R)(kR)^4 \ll 1$.

Finally, we notice that the opposite situation, where $\Delta u_{\parallel} \gg u$ is commonly used for optical chromatography, i.e. longitudinal segregation within flowing multi-component suspensions driven by cross-section-dependent light scattering (Kaneta *et al.* 1997; Hart & Terray 2003).

1.2.2. *Transverse segregation*

Another possible cause of segregation of an illuminated suspension is the gradient force density $\boldsymbol{f}_g$, which tends to attract particles whose refractive index is larger than the one of the surrounding fluid n into the high-intensity regions. As shown by Harada & Asakura (1996) the expression of the net gradient force $\boldsymbol{F}_g$ exerted on a single small spherical particle ($R \ll \lambda$) takes a simple form when $\Delta n \ll 1$, namely $\boldsymbol{F}_g = (2\pi R^3/3)(\Delta n/n)(\nabla I/c)$. Its transverse component thus scales as $(\Delta n/n)R^3(I/cw_0)$. Apart from its application to individual particle trapping (optical tweezers; see Padgett, Molloy & McGloin 2009), the gradient force also underlies of large optical nonlinearities of suspensions that are involved in self-focusing (Ashkin, Dziedzic & Smith 1982) or phase conjugation (Smith, Maloney & Ashkin 1982) phenomena.

Since suitable suspensions for light-induced flow experiments correspond to rather high concentrations of scatterers (see conditions (1.1) and (1.2)), their transverse segregation may be described as a diffusion process under the action of the gradient force. By so doing, a noticeable transverse gradient of concentration of scatterers

appears during the flow of the suspension on the distance L if the characteristic time scale t_d of Brownian diffusion of the particles on the distance w_0 due to the gradient force is shorter than L/u. Typically, we have $t_d = w_0^2/D$, where D is their diffusion coefficient, whose order of magnitude is given by the Einstein–Smoluchowski relation $D = k_B T/6\pi\eta R$, with k_B the Boltzmann's constant and T the temperature. Collective transverse segregation of the suspension therefore has no time to settle during the flow if $t_d \gg L/u$, which can be rewritten as

$$I \gg \frac{k_B T}{6\pi} \frac{Lc}{\tau n R w_0^4}, \tag{1.3}$$

a kinetic condition that involves the beam intensity. Alternatively, the amplitude of the transverse segregation can be determined by the balance between the diffusive flux density $\boldsymbol{j}_d$ of particles associated with the transverse gradient of concentration and the opposite flux density of particles due to the gradient force $\boldsymbol{j}_g$. On the one hand, we have $j_d \sim D\delta N/w_0$, where δN is the transverse variation of N. On the other hand, $\boldsymbol{j}_g = N\Delta\boldsymbol{u}_\perp$, where $\Delta\boldsymbol{u}_\perp = \boldsymbol{F}_g/6\pi\eta R$ is the particle transverse drift velocity. Recalling that $\Phi \sim NR^3$, the transverse variation of Φ, $\delta\Phi$, is obtained from $j_d \sim j_g$, which gives

$$\frac{\delta\Phi}{\Phi} \sim \frac{2\pi R^3}{3k_B T} \frac{I}{c} \frac{\Delta n}{n}, \tag{1.4}$$

a thermodynamic condition that also involves the beam intensity. Negligible transverse segregation thus corresponds to $\delta\Phi/\Phi \ll 1$, which can be rewritten as

$$I \ll \frac{3k_B T c}{2\pi R^3} \frac{n}{\Delta n}. \tag{1.5}$$

Notice that $\delta\Phi/\Phi$ can be rewritten in a more general form that emphasizes the key role played by the osmotic compressibility of the suspension, $\kappa_T = (\partial N/\partial\mathfrak{P})/N|_T$, where $\mathfrak{P}$ is its osmotic pressure. Since the local osmotic equilibrium $\nabla\mathfrak{P} = N\boldsymbol{F}_g$ is the analogue of the condition of local hydrostatic equilibrium in pure compressible fluids, we indeed obtain

$$\frac{\delta\Phi}{\Phi} \sim \frac{2\pi R^3}{3} \frac{I}{c} \frac{\Delta n}{n} N\kappa_T. \tag{1.6}$$

One can check that the condition (1.5) is also retrieved from (1.6) in the case of ideal mixtures, for which $N\kappa_T = (k_B T)^{-1}$.

When transverse segregation cannot be neglected, it may induce scattering force density gradients since the turbidity τ explicitly depends on the volume fraction Φ. It should therefore be taken into account for any quantitative analysis of experimental measurements.

1.2.3. *Conclusion and relevance of the present study*

When the above conditions under which a suspension flow induced by light scattering can be considered as homogeneous are not fulfilled, segregation phenomena must be described simultaneously with the flow. The sensitivity of the light-induced hydrodynamics of a suspension to its thermodynamic and rheological properties is well illustrated by (1.6), where κ_T can strongly differ from $(k_B T)^{-1}$ when the suspended scatterers do not behave ideally, for example in multi-component liquid mixtures.

In addition to the lack of theoretical description of light-induced hydrodynamics, very few quantitative experimental studies of light-driven bulk flows of scattering suspensions have been performed. Even a direct experimental proof of a bulk flow induced by the scattering force density in a suspension is lacking.

The first indirect proof of a light-induced bulk flow within a scattering fluid has been given in Schroll *et al.* (2007) by using a near-critical binary liquid mixture in the two-phase regime. It consists in the observation of broad (compared to w_0) deformations of the interface between the coexisting phases induced by an upward vertical laser beam impinging on the sample from the phase of lowest refractive index. These experimental results have been compared with their theoretical prediction based on drastic assumptions: (i) the two-layer liquid sample was described by a single phase, the bottom one, bounded by free surfaces; (ii) the broad surface deformations were considered to originate only from the bulk creeping flow induced by the laser beam; (iii) the observed slender 'nipple-like' interface deformation due to the radiation pressure, whose width is of the order of w_0, oriented in a direction opposite to the broad deformation formed by the bulk flow, was assumed to have no influence on the broad deformation or the flow. Although satisfactory agreement between experiments and theory has been obtained in Schroll *et al.* (2007), the comparison remained only semi-quantitative. Moreover, the existence of a bulk flow could not be directly demonstrated in this experimental configuration.

On the other hand, puzzling observations of the deformations of the free surface of a colloidal suspension of submicrometric latex spheres under pulsed illumination have been reported in Mitani & Sakai (2005). These results have been interpreted as a change of the liquid pressure beneath the surface due to an osmotic pressure contribution associated with steady segregation of the scatterers by the scattering force. The possible effect of a flow has thus been discarded, although the condition $\Delta u_{\parallel} \ll u$ given by (1.1) was satisfied. Such a controversial interpretation reinforces the need for an experiment providing a direct proof of the bulk flow induced by light scattering.

Given the above considerations, the use of a fluid near a critical point (near-critical fluid) constitutes an attractive alternative to non-absorbing, light scattering suspensions. At thermodynamic equilibrium, a near-critical fluid displays spatial and temporal fluctuations of composition (i.e. of refractive index) whose size increases in a well-documented manner as the critical point is approached (Sengers & Levelt-Sengers 1978), leading to the well-known phenomenon of 'critical opalescence'. These fluctuations may be viewed as a distribution of light scatterers whose submicrometric size can be tuned with temperature. Since these fluctuations take place in the whole fluid, such a fluid always satisfies the condition (1.1) and is thus expected to flow as a whole under the action of a light beam. Moreover, although the turbidity strongly varies with temperature, the condition of optical transparency given by (1.2) is actually always satisfied in our experiments, as shown in the next section.

Finally, transverse gradients of composition due to electrostriction (i.e. gradient force-induced segregation) and to thermodiffusion (Soret effect) induced by the beam result in negligible transverse variations of the refractive index δn and of the turbidity $\delta\tau$ of the microemulsion, as discussed in § 7.3.

This paper is organized as follows. In § 2, we present the equilibrium and transport properties of the two-phase near-critical binary liquid mixture that we used. The description of the experiment and a first qualitative observation of the jet are presented in § 3. This allows us to identify the characteristic features of the jet shape, the propagation of light inside it, and the light-induced flow. Then we demonstrate in § 4 that the beam propagation, the jet shape and the flow, which are *a priori* coupled, can in fact be partially decoupled. In § 5, we show that the measured jet diameter can be quantitatively described as the result of the balance between Laplace pressure and radiation pressure following a liquid optical fibre model (Brasselet & Delville

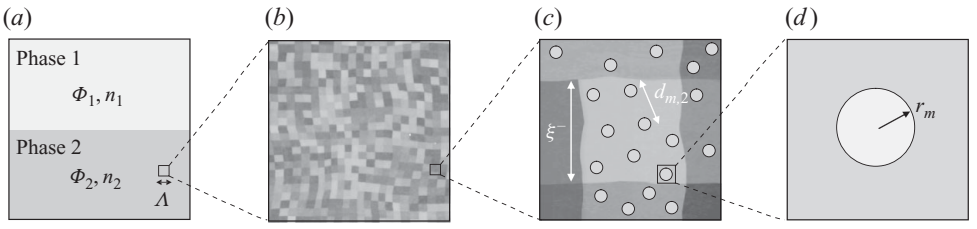

FIGURE 3. (*a*) Sketch of a sample of near-critical two-phase microemulsion. Each phase i, $i = 1, 2$ is characterized by a well-defined value of the volume fraction of droplets Φ_i, of the average distance between droplets $d_{m,i}$ and of the refractive index n_i. The double-arrow indicates the characteristic size Λ of the fluid element used to describe the flow of the microemulsion as well as Maxwell's electromagnetic stress tensor: see § 4. (*b*) Magnification showing the subwavelength fluctuations of the volume fraction of droplets and of the refractive index existing in each phase at thermodynamic equilibrium. These fluctuations induce light scattering. (*c*) Further magnification on a fluctuation of the volume fraction of droplets of characteristic size ξ^- common to both phases. The average distance between the droplets, $d_{m,2}$, is indicated. As the sample temperature T approaches its critical temperature T_c, ξ^- diverges whereas Φ_i (resp. $d_{m,i}$), $i = 1, 2$, both tend towards the same value $\Phi_c = 0.11$ (resp. $d_{m,c} = 13$ nm). In the investigated temperature range, ξ^- varies within the range 14–47 nm. (*d*) Further magnification on a single droplet of constant radius $r_m = 4$ nm.

2008). Consequently, we come to the conclusion there is no significant feedback of the light-induced flow on the jet shape or the beam propagation. Next, in § 6, we describe the flow as a parallel creeping flow driven solely by the scattering force density associated with the light guided along the jet. In § 7 we present the dripping flow rate measurements, which are compared to our theoretical predictions. Finally, we discuss the obtained agreement between experiment and theory.

2. Equilibrium and transport properties of the liquid sample

Our sample is a near-critical fluid that consists of a quaternary mixture of toluene (mass fraction 69.6 %), water (9.34 %), sodium dodecyl sulphate (SDS, 4.31 %) as surfactant and n-butanol (16.75 %) as co-surfactant. For this composition its equilibrium state is a water-in-oil droplet microemulsion (hereafter *microemulsion* for simplicity), i.e. a thermodynamically stable suspension of droplets within a continuous phase composed of toluene and alcohol. The droplets are stabilized by surfactant and are made of water (principally), alcohol and SDS. Their characteristic radius r_m is 4 nm, as sketched in figure 3(*d*). Moreover, for this composition, the microemulsion is close to a consolute line at room temperature and undergoes a critical behaviour. In the vicinity of the critical temperature $T_c = 308$ K, this quaternary mixture behaves as a critical binary mixture, the volume fraction of droplets Φ being the order parameter of the second-order phase transition. For a temperature $T < T_c$ the sample is one-phase. For $T > T_c$ the sample, sketched in figure 3(*a*), is two-phase, the upper phase of index 1 (respectively, the lower phase of index 2) being the phase of smallest (resp. largest) volume fraction of droplets Φ_1 (resp. Φ_2) and of largest (resp. smallest) refractive index n_1 (resp. n_2). The composition is chosen such that the sample separates into two phases of equal volumes at $T = T_c$. This corresponds to an average volume fraction of droplets of the sample $\Phi = 0.11$ equal to its critical value Φ_c. The average distance between the droplets is $d_{m,i} = (4\pi/(3\Phi_i))^{1/3} r_m$, $i = 1, 2, c$, and weakly departs from $d_{m,c} = 13$ nm in the investigated temperature range.

As the critical consolute line is approached, the isothermal osmotic susceptibility of the microemulsion $\chi_T = (\partial\Phi/\partial\mu)|_T$ (μ is the chemical potential) diverges. This induces the divergence of the correlation length ξ of the fluctuations of the order parameter, i.e. of the size of the fluctuations of the volume fraction of droplets, sketched in figure 3(*b*, *c*). Given the isotropy of the microemulsion and the temperature range investigated here, $\Delta T = T - T_c = 2$–$15\,\mathrm{K}$, the thermophysical properties of the two-phase sample are assumed to obey the asymptotic scaling laws of critical phenomena of the universality class ($d = 3$, $n = 1$) of the Ising model, where d and n are here, respectively, the space and order parameter dimensionality (Sengers & Levelt-Sengers 1978). Namely, χ_T and ξ are assumed to diverge at the critical temperature following

$$\chi_T^{\pm} = \chi_{T0}^{\pm} \left(\frac{|\Delta T|}{T_c} \right)^{-\gamma}, \tag{2.1}$$

$$\xi^{\pm} = \xi_0^{\pm} \left(\frac{|\Delta T|}{T_c} \right)^{-\nu}, \tag{2.2}$$

with $\gamma = 1.24$, $\nu = 0.63$, $\xi_0^+ = 4\,\mathrm{nm}$, $\chi_{T0}^+ = 5.78 \times 10^{-6}\,\mathrm{Pa}^{-1}$ (see Appendix A), $\chi_{T0}^+/\chi_{T0}^- = 4.3 \pm 0.3$ and $\xi_0^+/\xi_0^- = 1.9 \pm 0.2$ (Beysens, Bourgou & Calmettes 1982). The scaling laws (2.1) and (2.2) written with index + (resp. −) are valid in the one-phase region (resp. for each phase in the two-phase region) (Moldover 1985; Beysens *et al.* 1982). Typical values of ξ^- encountered in the experiments range from 47 nm at $\Delta T = 2\,\mathrm{K}$ to 14 nm at $\Delta T = 15\,\mathrm{K}$.

Assuming, for simplicity, the coexistence curve to be symmetric with respect to Φ_c, we get

$$\Phi_i = \Phi_c + (-1)^i \frac{\Delta\Phi_0}{2} \left(\frac{\Delta T}{T_c} \right)^{\beta}, \quad i = 1, 2, \tag{2.3}$$

with $\beta = 0.325$ and $\Delta\Phi_0 = 0.42$, an effective value determined from a careful study of the small-amplitude interface deformations induced by radiation pressure in Chraïbi *et al.* (2008*a*).

Since the average distance between the droplets is small compared to the optical wavelength, a simple expression for the effective relative dielectric permittivity ε of the suspension can be derived from a mean field calculation. For this purpose, we introduce the relative dielectric permittivities of the mixture composing a droplet and the continuous phase, $\varepsilon_{drop} = 1.86$ and $\varepsilon_{cont} = 2.14$, respectively. It is known that, to leading order in $|\varepsilon_{cont} - \varepsilon_{drop}|/(\varepsilon_{cont} + \varepsilon_{drop})$, the relationship between ε and Φ for each phase is (Landau, Lifshitz & Pitayevski 1984)

$$\varepsilon_i = \Phi_i \varepsilon_{drop} + (1 - \Phi_i)\varepsilon_{cont} - \frac{\Phi_i(1 - \Phi_i)(\varepsilon_{drop} - \varepsilon_{cont})^2}{3(\Phi_i \varepsilon_{drop} + (1 - \Phi_i)\varepsilon_{cont})}, \quad i = 1, 2. \tag{2.4}$$

The corresponding refractive indices are obtained using $n_i = \sqrt{\varepsilon_i}$. Typical values for the refractive index difference $n_1 - n_2$ encountered in the present experiments range from 8.2×10^{-3} at $\Delta T = 2\,\mathrm{K}$ to 1.6×10^{-2} at $\Delta T = 15\,\mathrm{K}$.

The interfacial tension σ, defined for $T > T_c$, vanishes at T_c following

$$\sigma = \sigma_0 \left(\frac{\Delta T}{T_c} \right)^{2\nu}, \tag{2.5}$$

where $\sigma_0 = 0.39 k_B T_c/\xi_0^{+2} = 10^{-4}\,\mathrm{N\,m^{-1}}$ (Moldover 1985; Casner & Delville 2001). Typical values of σ encountered in the experiments range from $1.8 \times 10^{-7}\,\mathrm{N\,m^{-1}}$ at $\Delta T = 2\,\mathrm{K}$ to $2.3 \times 10^{-6}\,\mathrm{N\,m^{-1}}$ at $\Delta T = 15\,\mathrm{K}$.

Concerning the rheological properties of the microemulsion, the volume fraction of droplets in each liquid phase is small enough to assume a Newtonian behaviour (viscoelastic effects are indeed noticeable at volume fraction of droplets larger than 0.3; Cametti *et al.* 1990). The viscosity values of each phase in the two-phase region are extrapolated from the measurements performed in the one-phase region near $T = T_c$ by Freysz (1990). This is done by using Einstein's relationship, which is valid for low-volume fraction suspensions of solid spheres (this seemingly rough choice is justified in Appendix A):

$$\eta_i(\mathrm{mPa \cdot s}) = (1.460 - 0.014T(^\circ\mathrm{C}))(1 + 2.5\Phi_i), \quad i = 1, 2. \tag{2.6}$$

Finally, we notice that the optical absorption coefficient α_{abs} at wavelength $\lambda_0 = 514.5\,\mathrm{nm}$ in vacuum is very small, $\alpha_{abs} \sim 5.10^{-2}\,\mathrm{m}^{-1}$ (Jean-Jean *et al.* 1988).

3. Characteristic features of the jet

3.1. *Experimental set-up*

The two-phase sample of near-critical microemulsion is enclosed in a fused quartz cell of height $h = 2\,\mathrm{mm}$ and $10\,\mathrm{mm} \times 40\,\mathrm{mm}$ horizontal cross-section (see figure 1*b*). Its temperature T is regulated with a 50 mK accuracy in the range 2–15 K above T_c. In this study, we investigate a set of temperatures that correspond to $\Delta T = 2$, 4, 8, 12 and 15 K.

The light source is a linearly polarized beam obtained from a continuous wave Ar^+ laser operating in the TEM_{00} mode at $\lambda_0 = 514.5\,\mathrm{nm}$. The laser beam propagates vertically downwards along z and is focused on the horizontal liquid interface of the sample that is located at the half-height of the cell. In the cylindrical coordinates system defined by the unit vectors $(\hat{\boldsymbol{r}}, \hat{\boldsymbol{\theta}}, \hat{\boldsymbol{z}})$, the intensity distribution of the beam cross-section at the interface is

$$I(r) = \frac{2\mathscr{P}}{\pi w_0^2} \exp\left(\frac{-2r^2}{w_0^2}\right), \tag{3.1}$$

where $\mathscr{P}$ is the total beam power and w_0 the beam waist that is set to 3.47 μm in this study.

Finally, the interface deformations are observed in transmission using a CCD camera using a white light side illumination. Although small, the turbidity of the sample may reduce the sharpness of the interface image (blurring) if the distance between the laser beam and the cell side that faces the camera is too large. On the other hand, it is preferable to have it as large as possible in order to prevent unwanted non-axisymmetric drawbacks. A trade-off is found in practice by choosing such a distance to be roughly 50 μm.

3.2. *Qualitative observation of the light-induced jet*

At low power, the radiation pressure of the laser beam induces a bell-shaped deformation whose height increases with the beam power. At a given power threshold (Casner & Delville 2003) the deformation profile suddenly changes to a vertical needle-like deformation with diameter d of the order of w_0 and length of the order of several tens of w_0. Moreover, the needle tip continuously emits droplets, as shown in figure 4(*b*).

By inserting a thick birefringent crystal between the sample cell and the camera and suitable beam polarization adjustment it is possible to simultaneously acquire on the CCD two different pictures of the same experiment: the jet superimposed on the

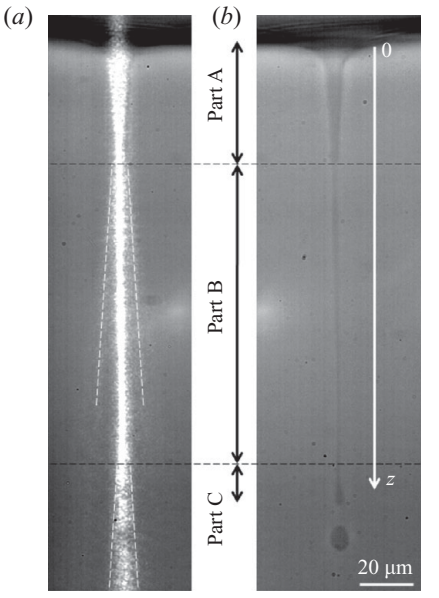

FIGURE 4. Simultaneous imaging of the shadow of the jet superimposed on the laser light scattered towards the camera (a) and of the shadow of the jet alone (b). The jet can be divided into three parts to which we, respectively, refer to as parts A, B and C. See the text for a detailed analysis of each of these parts. Experimental conditions are $w_0 = 3.47\,\mu\text{m}$, $\Delta T = 8\,\text{K}$ and $\mathscr{P} = 350\,\text{mW}$.

laser light scattered by the refractive index fluctuations of the sample and the shadow of the jet alone obtained by refraction of the white light. Such a double picture is shown in figure 4. In fact, the simultaneous visual inspection of both the jet shape and the distribution of light intensity within it reveals the guiding of the light within the jet. Wave guiding is indeed a consequence of the inequality $n_1 > n_2$, which implies total internal reflection of light on the jet boundary.

One can distinguish three parts along the jet: the beam injection funnel, A, the cylindrical guiding part, B, and the tip emitting droplets, C. Along part A, the interface shape continuously evolves from a flat interface to a cylinder and the light beam exhibits a conical intensity distribution showing its progressive focusing into the jet. A cone of light outlined by dotted lines originating from the A–B boundary shows that a part of the incident light is not guided by part B. Along part B the laser light intensity distribution is invariant along z and the jet is straight and cylindrical, as a result of the guiding of light by the jet. At the beginning of part C the beam is no longer guided, as shown by its sudden spreading by diffraction outlined by dotted lines. Then, the jet undulates downwards and breaks into regularly detaching droplets. Such a continuous dripping jet phenomenon reveals that a steady flow takes place inside the jet. Notice finally, that the jet length (Wunenburger, Casner & Delville 2006*b*), its diameter and the flow rate all increase with the beam power.

Experimentally, we will use the fact that the flow rate of the dripping jet is equal to the flow rate inside part B of the jet. Moreover, when considering the quantitative description of the flow rate inside the jet, we will benefit from the above qualitative observations. In particular, we will derive a model that describes the beam propagation, the flow and their coupling.

4. Model of coupled beam propagation, jet shape and flow

Achieving a tractable theoretical model of the above-mentioned experimental observations requires an accurate description of the beam propagation, the jet shape and the flow. First, we present the equations describing the velocity, pressure and electromagnetic force fields associated with the observed jet shape and flow, which turn out to be decoupled in part B of the jet (see figure 4).

Since the observed flow is characterized by a small Reynolds number $Re \sim 10^{-4}$ (see § 7), we assume that a creeping, incompressible, steady flow driven by light develops in each liquid phase. The fluid under study is a microemulsion, i.e. a two-phase fluid from the point of view of both hydrodynamics and electromagnetism. So, the description of its composition, of its flow, and of the electromagnetic forces exerted on it strongly depends on the characteristic size of the fluid element considered for their definition in the framework of continuum mechanics and electrodynamics, i.e. on the length scale Λ over which they are averaged. Since $\lambda = \lambda_0/n_c \simeq 350\,\text{nm}$, where $n_c = 1.464$ is the refractive index of the microemulsion in the one-phase region, and due to the fact that ξ^- varies in the range 14–47 nm and $d_{m,i} \simeq 13\,\text{nm}$, we have $\lambda \gg \xi^- > d_{m,i}$. Consequently we can choose Λ such that $\lambda > \Lambda \gg \xi^-$. This choice allows us to write the equation of conservation of momentum in the Stokes regime in the following form:

$$\mathbf{0} = \boldsymbol{f}_i^{hydro} + \boldsymbol{f}_i^{em} + \boldsymbol{f}_i^{scatt}, \quad i = 1, 2. \tag{4.1}$$

Here, $\boldsymbol{f}_i^{hydro}$ is the classical hydrodynamic force per unit volume exerted on each fluid phase i considered to be homogeneous since $\Lambda \gg \xi^-$. $\boldsymbol{f}_i^{em}$ is the electromagnetic force density exerted on each phase i considered as a perfect isotropic dielectric that is homogeneous at the scale of the spatial variations of the electric field λ since $\lambda > \Lambda \gg \xi^-$. $\boldsymbol{f}_i^{scatt}$ is the scattering force density associated with the scattering of light by the subwavelength refractive index fluctuations that actually drives the flow.

In agreement with the condition $\Lambda \gg \xi^-$, we assume that, as far as their flow is concerned, each phase behaves as a homogeneous, Newtonian fluid at the scale of Λ. Consequently, $\boldsymbol{f}_i^{hydro}$ can be expressed as the divergence of the classical hydrodynamic stress tensor $\boldsymbol{T}_i^{hydro} = -p_i \boldsymbol{I} + 2\eta_i \boldsymbol{D}(\boldsymbol{v}_i)$, where $\boldsymbol{v}_i$ and p_i are, respectively, the velocity and the pressure of liquid phase i, $\boldsymbol{I}$ is the identity tensor, η_i the viscosity of the suspension defined by (2.6), and $\boldsymbol{D}(\boldsymbol{v}) = (\nabla \boldsymbol{v} + {}^t\nabla \boldsymbol{v})/2$ is the hydrodynamic strain rate tensor valid for incompressible flows, i.e. for which $\nabla \cdot \boldsymbol{v} = 0$, where ${}^t(\ldots)$ refers to the transpose operator.

In the following, we justify and specify the expression of the electromagnetic forces as the sum of $\boldsymbol{f}_i^{em}$ and $\boldsymbol{f}_i^{scatt}$.

4.1. *Electromagnetic force density under homogeneous medium approximation*

Since $\Lambda \gg \xi^- > d_m$, the effective relative dielectric permittivity ε_i of each liquid phase i at the scale Λ is given by (2.4). The force density $\boldsymbol{f}^{em}$ exerted on a dielectric homogeneous fluid can be expressed as the divergence of the Maxwell electromagnetic stress tensor $\boldsymbol{T}^{em}$ provided that the relative dielectric permittivity and the density of the fluid are homogeneous at the scale of the spatial variations of the electric field $\boldsymbol{E}$, i.e. λ (Landau *et al.* 1984). Since $\Lambda < \lambda$, this condition is fulfilled, which allows us to assume that the electromagnetic force density exerted on each liquid phase incorporates a contribution $\boldsymbol{f}_i^{em}$ defined as the divergence of

$$\boldsymbol{T}_i^{em} = \frac{1}{2}\varepsilon_0 \rho_i \left.\frac{\partial \varepsilon_i}{\partial \rho_i}\right|_T \boldsymbol{E}^2 \boldsymbol{I} - \frac{1}{2}\varepsilon_0 \varepsilon_i \boldsymbol{E}^2 \boldsymbol{I} + \varepsilon_0 \varepsilon_i \boldsymbol{E}\, {}^t\boldsymbol{E}, \quad i = 1, 2, \tag{4.2}$$

where ε_i and ρ_i are the effective relative dielectric permittivity and average density of the liquid phase defined at the scale Λ, ε_0 is the dielectric permittivity of vacuum. In (4.2) and in the following, all quantities involving the electric field are implicitly time-averaged over one optical period.

The first term of (4.2) is usually called the 'electrostriction term'. Noting that the force density associated with the two last terms of (4.2) can be written as $\boldsymbol{\nabla}\cdot(\varepsilon_0\varepsilon\boldsymbol{E}^t\boldsymbol{E}-\varepsilon_0\varepsilon\boldsymbol{E}^2\boldsymbol{I}/2)=-\varepsilon_0\boldsymbol{E}^2\boldsymbol{\nabla}\varepsilon/2$ (Landau *et al.* 1984), we conclude that it cancels in the bulk of both liquid phases since they are considered as having a homogeneous dielectric constant.

Introducing the pseudo-pressures $q_i = p_i - \varepsilon_0\boldsymbol{E}_i^2\rho_i/2(\partial\varepsilon_i/\partial\rho_i)\big|_T$ and using the flow incompressibility and liquid phase homogeneity assumptions, (4.1) becomes

$$\boldsymbol{0} = -\boldsymbol{\nabla}q_i + \eta_i\Delta\boldsymbol{v}_i + \boldsymbol{f}_i^{scatt}, \quad i = 1, 2. \tag{4.3}$$

Since $\boldsymbol{f}^{scatt}$ is due to the scattering of light by finite refractive index fluctuations of characteristic size $\xi^- \ll \Lambda$, its derivation requires a description of the propagation of light and of the fluid using a length scale smaller than Λ. This is the aim of the next section.

4.2. *The scattering force density*

In this section, we derive the expression of the scattering force density $\boldsymbol{f}^{scatt}$ by describing the microemulsion and the electromagnetic field on a scale Λ^{scatt} that is much smaller than the characteristic size of the refractive index inhomogeneities, ξ^-.

In the case of a spherical particle of radius R such that $R \ll \lambda$, it has been shown that both the corpuscular approach and the continuum electrodynamics approach based on the electromagnetic tensor predict the same expression for the scattering force exerted on an individual particle (Nieto-Vesperinas, Chaumet & Rahmani 2009). In the case of a near-critical fluid, it is usual to describe the scatterers in terms of a continuously varying refractive index field characterized by a correlation length ξ^- that diverges at the critical temperature (see Appendix A). Here we combine the latter framework to the above-mentioned corpuscular approach in order to derive the scattering force $\boldsymbol{f}^{scatt}$ exerted on the microemulsion.

First, we assume that the absorption of light is weak and can be neglected. Therefore, the force per unit volume exerted on the microemulsion is solely due to the elastic scattering of the incident light by the refractive index fluctuations. As discussed in § 1.2, the scattering force density exerted on a fluid by a light beam is equal to the loss of momentum per unit cross-section area and per unit time of the beam associated with its propagation through the fluid over a unit distance. The scattering force density is related to the turbidity τ, which is the relative loss of intensity of the beam per unit propagation length. Noting that $I^{-1}(\mathrm{d}^2I/\mathrm{d}\Omega\mathrm{d}z)(\Omega)\,\mathrm{d}\Omega$ is the relative intensity scattered per unit length in the solid angle $\mathrm{d}\Omega$ centred on the direction Ω, the turbidity is defined as

$$\tau = \iint \frac{1}{I}\frac{\mathrm{d}^2I}{\mathrm{d}\Omega\,\mathrm{d}z}(\Omega)\,\mathrm{d}\Omega. \tag{4.4}$$

The momentum flux density associated with the light scattered in the direction of unit vector $\boldsymbol{u}$ is $(nI/c)\boldsymbol{u}$, where n is the average fluid refractive index and I the light intensity. Consequently, the scattering force density can be written as

$$\boldsymbol{f}^{scatt} = -\iint \frac{n}{c}\frac{\mathrm{d}^2I}{\mathrm{d}\Omega\,\mathrm{d}z}(\Omega)\boldsymbol{u}_\Omega\,\mathrm{d}\Omega, \tag{4.5}$$

where $\boldsymbol{u}_{\Omega}$ is the unit vector associated with the direction Ω. Using Ornstein and Zernike's theory of light scattering by critical fluctuations (Ornstein & Zernike 1914), Puglielli & Ford (1970) calculated the turbidity of a near-critical pure fluid from (4.4) (see Appendix A). Schroll *et al.* (2007) used (4.5) to calculate the scattering force density in a near-critical binary mixture:

$$\boldsymbol{f}_i^{scatt} = \frac{\pi^3}{\lambda_0^4}\frac{n_i I_i}{c}\left(\left.\frac{\partial \varepsilon_i}{\partial \Phi_i}\right|_T\right)^2 k_B T \chi_T g(\alpha_i)\hat{\boldsymbol{z}}, \quad i = 1, 2, \tag{4.6}$$

where $\alpha_i = 2(k_i\xi^-)^2$, $k_i = 2\pi n_i/\lambda_0$ being the wavenumber of the incident monochromatic beam and

$$g(\alpha_i) = \frac{\frac{8}{3}\alpha_i^3 + 2\alpha_i^2 + 2\alpha_i - \left(2\alpha_i^2 + 2\alpha_i + 1\right)\ln(1 + 2\alpha_i)}{\alpha_i^4}, \quad i = 1, 2 \tag{4.7}$$

The order of magnitude of the scattering force density involved in our experiments is inferred from the relationship $f^{scatt} \simeq \tau I n/c$. The turbidity of the near-critical microemulsion measured by Freysz (1990) in the one-phase region, in the same range of ΔT as used here, has been found to be of the order of 100–300 m^{-1} (see Appendix A). In addition, the turbidity in the two-phase region is approximately 4 times smaller than in the one-phase region (see (2.1)). Consequently, in the two-phase region, the typical values of the turbidity range between 25 and 75 m^{-1}. Notice that $\tau \gg \alpha_{abs}$, confirming that the light-induced force density actually originates mainly from light scattering. Using $\langle n \rangle = 1.464$ as a characteristic value for the refractive index and $I \sim 2\mathscr{P}/\pi w_0^2$ with $\mathscr{P} = 0.1 - 1\,\mathrm{W}$, we find $f^{scatt}/I \sim 10^{-7} - 4 \times 10^{-7}\,\mathrm{N\,W^{-1}\,m^{-1}}$ and $f^{scatt} \simeq 6 \times 10^2 - 2 \times 10^4\,\mathrm{N\,m^{-3}}$. The exact variations of f_i^{scatt}/I as a function of temperature predicted by (4.6) confirm this rough estimate. For $\alpha \ll 1$, i.e. far from the critical point, $g(\alpha) \simeq 8/3$ and the scattering force scales as $(|\Delta T|/T_c)^{-\gamma}$ (in particular, we recover that f^{scatt} vanishes for vanishing size of the refractive index fluctuations). Close to the critical point $\alpha \gg 1$ ($\alpha > 1$ in the temperature range $\Delta T < 8\,\mathrm{K}$), so $g(\alpha) \sim \alpha^{-1} \sim (|\Delta T|/T_c)^{2\nu}$ and consequently $f^{scatt} \sim (|\Delta T|/T_c)^{-\gamma+2\nu} \sim (|\Delta T|/T_c)^{0.02}$: the scattering force becomes practically independent of ΔT. Notice that f^{scatt} takes practically the same values in both phases in the investigated temperature range since the material properties of the phases do not differ much.

4.3. *Force balance at the interface*

Finally, the flow equation (4.3) expressed in both phases has to be completed by the expression of the balance of the forces exerted on the interface between fluids 1 and 2. Assuming a uniform interfacial tension σ and using Λ as the characteristic length scale of the description of the liquid phases and of the interface, this force balance can be written as

$$\left(\boldsymbol{T}_2^{hydro} - \boldsymbol{T}_1^{hydro}\right)\boldsymbol{n}_{1\to 2} + \left(\boldsymbol{T}_2^{em} - \boldsymbol{T}_1^{em}\right)\boldsymbol{n}_{1\to 2} - \sigma\kappa\boldsymbol{n}_{1\to 2} = \boldsymbol{0}, \tag{4.8}$$

where $\boldsymbol{n}_{1\to 2}$ is the unit vector normal to the interface oriented from 1 to 2 and κ the interface curvature, all the tensors being evaluated at the interface. Introducing the pseudo-pressures, (4.8) can be rewritten as

$$\begin{aligned}(q_1 - q_2)\boldsymbol{n}_{1\to 2} &+ \left[\eta_2 \boldsymbol{D}_2(\boldsymbol{v}_2)\boldsymbol{n}_{1\to 2} - \eta_1 \boldsymbol{D}_1(\boldsymbol{v}_1)\boldsymbol{n}_{1\to 2}\right] \\ &+ \left[\varepsilon_0\varepsilon_2\left(\boldsymbol{E}_2\,{}^t\boldsymbol{E}_2\right)\cdot\boldsymbol{n}_{1\to 2} - \varepsilon_0\varepsilon_1\left(\boldsymbol{E}_1\,{}^t\boldsymbol{E}_1\right)\cdot\boldsymbol{n}_{1\to 2}\right] \\ &- \tfrac{1}{2}\left(\varepsilon_0\varepsilon_2\boldsymbol{E}_2^2 - \varepsilon_0\varepsilon_1\boldsymbol{E}_1^2\right)\boldsymbol{n}_{1\to 2} = \sigma\kappa\boldsymbol{n}_{1\to 2}.\end{aligned} \tag{4.9}$$

The latter expression calls for two remarks.

(i) Equations (4.3) and (4.9) do not involve the electrostriction term of (4.2). Consequently, the incompressible flow is independent of the electrostriction that modifies the pressure field within each liquid phase, but without associated stress at the jet boundary. In (4.3) the scattering force density thus appears as the only driving force of the flow, which *a posteriori* justifies its introduction in (4.1).

(ii) The interfacial stress that results from the two last terms of the left-hand side of (4.9) represents the radiation pressure in the formalism of continuum electrodynamics. As shown in Appendix B, this interfacial stress is always normal to the interface between two dielectrics, which we will therefore refer to as $\Pi\hat{\boldsymbol{r}}$ since $\hat{\boldsymbol{r}}$ identifies with $\boldsymbol{n}_{1\to2}$ in part B of the jet.

4.4. *Decoupling the jet shape and the flow*

In this section, we show that the equations governing the jet shape (4.9) and the flow (4.3) can be partly decoupled.

As shown in figure 4, the jet shape and the light distribution of light within the jet are both invariant by translation along z in part B. Consequently, we describe the latter as a cylinder of circular cross-section and radius R_1. This implies that we can consider (i) the flow as a creeping incompressible steady parallel axial flow invariant along z, $\boldsymbol{v}_i = v_i(r)\hat{\boldsymbol{z}}$ $(i=1,2)$, and (ii) the propagation of light as the optical wave guiding of an incident beam entering a step-index cylindrical fibre of circular cross-section and radius R_1.

Since in the investigated temperature range $\tau \sim 25$–$75\,\mathrm{m}^{-1}$, the attenuation of the beam intensity along the jet of typical length 200 μm is estimated to range between 0.5 and 1.5 %. Thus, the beam attenuation along part B due to light scattering is neglected. The electromagnetic field and the scattering force density are therefore chosen to be invariant along z and cylindrically symmetric, $\boldsymbol{E}_i = \boldsymbol{E}_i(r)$ and $\boldsymbol{f}_i^{scatt} = f_i^{scatt}(r)\hat{\boldsymbol{z}}$ $(i=1,2)$.

Following the above assumptions, the radial component of (4.3) satisfies $\partial q_i/\partial r = 0$. As a result, q_i, hence p_i, depend only on z. Then, the divergence of (4.3) gives $\mathrm{d}^2 q_i/\mathrm{d}z^2 = 0$, which implies that the axial pseudo-pressure gradient is constant in each phase, $\mathrm{d}q_i/\mathrm{d}z = C_i$. Far away from the beam (i.e. $r \gg w_0$) the liquid interface is flat at $z=0$ (see figure 1*a*) and the flow and the electromagnetic field are negligible. Therefore, (4.9) gives $q_1(z=0) = q_2(z=0) = p_0$, where p_0 is the pressure at $z=0$ in the absence of laser illumination. One finally gets $q_i(z) = p_0 + C_i z$. Moreover, the velocity field, the electromagnetic field and the jet radius, hence its curvature $\kappa = R_1^{-1}$, are assumed to be invariant along z. Therefore, the force balance at the jet boundary given by (4.9) implies that $q_1(z) - q_2(z)$ is independent of z. Consequently, $C_1 = C_2 = C$ and $q_1(z) - q_2(z) = 0$ for all z.

Finally, the approximation of axial and cylindrically symmetric flow implies that the balance of viscous forces at the interface is purely axial and, since $\boldsymbol{n}_{1\to2} = \hat{\boldsymbol{r}}$ for the vertical cylindrical jet interface of radius R_1, we have $\eta_2 \boldsymbol{D}_2(\boldsymbol{v}_2)\boldsymbol{n}_{1\to2} - \eta_1 \boldsymbol{D}_1(\boldsymbol{v}_1)\boldsymbol{n}_{1\to2} = [\eta_2(\mathrm{d}v_{z,2}/\mathrm{d}r)|_{r=R_1} - \eta_1(\mathrm{d}v_{z,1}/\mathrm{d}r)|_{r=R_1}]\hat{\boldsymbol{z}}$.

The above considerations lead to a useful simplified expression of the force balance at the interface, whose axial and radial projections are, respectively,

$$\eta_1 \left.\frac{\mathrm{d}v_{z,1}}{\mathrm{d}r}\right|_{r=R_1} = \eta_2 \left.\frac{\mathrm{d}v_{z,2}}{\mathrm{d}r}\right|_{r=R_1}, \tag{4.10}$$

$$\Pi = \frac{\sigma}{R_1}. \tag{4.11}$$

On the one hand, the axial force balance (4.10) does not explicitly involve the electromagnetic field, and the flow is therefore driven solely by the scattering force density. On the other hand, (4.11) shows that the radius of the jet is independent of the flow and is solely determined by the balance between the Laplace pressure and the electromagnetic radiation pressure. In other words, the wave guiding properties of the jet and the light propagation inside it are independent of the flow.

Summarizing, the observed invariance along z of part B of the jet results in a partial decoupling between the beam propagation, the jet shape and the flow. Although the jet shape and the beam propagation are strongly coupled through (4.11), they are independent of the flow. In practice, the jet radius and the electromagnetic field distribution in the core and cladding regions of the liquid optical fibre have to be determined first by solving (4.11). Then, the scattering force density field and the resulting flow inside and outside the jet can be determined.

5. Explaining the observed jet radius

5.1. *Modelling the coupling between the beam propagation and the jet shape*

Inside the jet of radius R_1, the light can be considered to be guided by a step-index liquid optical fibre with core radius R_1. As shown above, this radius is a solution of (4.11), which describes the static equilibrium of a liquid cylindrical interface under the action of the Laplace pressure and of the electromagnetic radiation pressure. This static equilibrium problem was originally solved (Brasselet & Delville 2008) in order to explain the optical stabilization of large-aspect-ratio liquid bridges (Brasselet *et al.* 2008). Hereafter we first briefly recall the main features of the model presented in detail in Brasselet & Delville (2008). Then, we successfully compare the measured jet radii to their values predicted using this model.

In order to determine the solutions of (4.11), we assume the jet to be a perfect cylinder of radius R_1 (see figure 5*a*), thereby neglecting part A of the jet, whose length is indeed short compared to the Rayleigh length of the beam, $\pi w_0^2/\lambda \simeq 100\,\mu\text{m}$. Consequently, the situation corresponds to an incident Gaussian beam with waist w_0 focused at $z=0$ at the entrance of a step-index fibre of radius R_1 with core and cladding refractive indices n_1 and n_2, respectively, as illustrated in figure 5(*a*). The electromagnetic field is thus expressed as a linear combination of only the propagating guided modes of a step-index dielectric waveguide, i.e. we exclude the evanescent and non-guided modes (Snyder & Love 1983) that are not invariant along z. Since the incident Gaussian beam is cylindrically symmetric and linearly polarized (say along $\hat{\boldsymbol{x}}$), only the guided modes having the same symmetry and polarization are considered (in the following, they are indexed by the integer $m \geqslant 1$). In the limit of weak guiding, $(n_1\text{–}n_2) \ll n_1$, an assumption that is well satisfied in our experiments, the complex electric field of the transverse component of the mode m is expressed as (Snyder & Love 1983)

$$\boldsymbol{E}_\perp^{(m)} = E_0^{(m)} \mathscr{R}^{(m)}(r) \mathrm{e}^{\mathrm{i}(\beta_m z - \omega t)} \hat{\boldsymbol{x}}, \tag{5.1}$$

where $E_0^{(m)}$ is its amplitude and $R^{(m)}(r)$ its r-dependent spatial modulation given by

$$\mathscr{R}_m(r) = \begin{cases} \dfrac{J_0(\kappa_m r)}{J_0(\kappa_m R_1)} & \text{if } r \leqslant R_1, \\ \dfrac{K_0(\gamma_m r)}{K_0(\gamma_m R_1)} & \text{if } r \geqslant R_1, \end{cases} \tag{5.2}$$

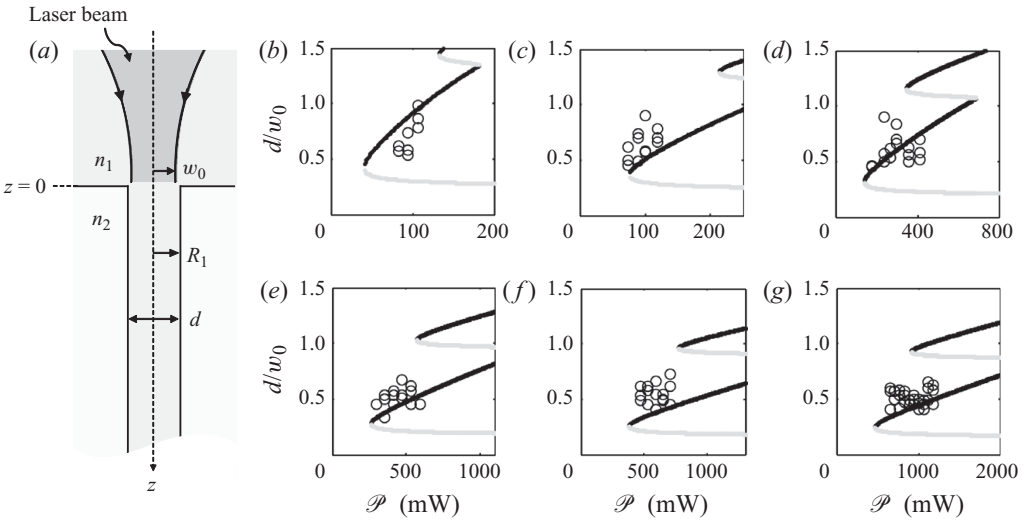

FIGURE 5. (*a*) Sketch of the simplified geometry assumed to describe the beam injection into the jet that acts as a liquid optical waveguide. (*b–g*) Solid, black (resp. grey) curves represent the calculated stable (resp. unstable) jet diameter d rescaled by the beam waist $w_0 = 3.47\,\mu\text{m}$ as function of the beam power $\mathscr{P}$ for $\Delta T = 1$ (*b*), 2 (*c*), 4 (*d*), 8 (*e*), 12 (*f*) and 15 K (*g*). Symbols: measured jet diameter.

where J_n and K_n are, respectively, the Bessel function of the first kind and the modified Bessel function of the second kind. The wavenumbers κ_m and γ_m are the mth roots of the characteristic equation

$$\kappa_m \frac{J_1(\kappa_m R_1)}{J_0(\kappa_m R_1)} = \gamma_m \frac{K_1(\gamma_m R_1)}{K_0(\gamma_m R_1)}, \tag{5.3}$$

with $(\kappa_m R_1)^2 + (\gamma_m R_1)^2 = k_0^2 R_1^2 (n_1^2 - n_2^2)$, where $k_0 = 2\pi/\lambda_0$. In addition, ω is the wave pulsation and β_m the propagation constant such that $\beta_m = (n_1^2 k_0^2 - \kappa_m^2)^{1/2} = (\gamma_m^2 - n_2^2 k_0^2)^{1/2}$.

For given values of n_1, n_2 and λ_0, the number of roots (κ_m, γ_m) of (5.3), hence the number of guided modes that propagates in the waveguide, depends on R_1. Below a threshold radius of the order of 1 µm under our experimental conditions, a single guided mode propagates along the waveguide, the mode $m = 1$. Such a monomodal behaviour is only valid for $R_1 < R_1^{(2)}$, where $R_1^{(2)}$ is the cutoff radius above which the mode $m = 2$ appears. Beyond $R_1^{(2)}$, the guided propagation is therefore multi-modal and the number of propagating guided modes increases with R_1. The respective contribution of each of these modes to the total field inside the jet is determined in practice by the fact that the guided modes constitute an orthogonal basis of the space of the guided propagating fields.

As shown in Appendix B, the radiation pressure exerted on the interface has the following expression:

$$\Pi = \frac{1}{4}\varepsilon_0 (n_1^2 - n_2^2)\left(|\boldsymbol{E}_{t,1}|^2 + \frac{n_1^2}{n_2^2}|\boldsymbol{E}_{n,1}|^2\right), \tag{5.4}$$

where $\boldsymbol{E}_{n,1} = (\boldsymbol{E}_1 \cdot \boldsymbol{n}_{1\to 2})\boldsymbol{n}_{1\to 2}$ and $\boldsymbol{E}_{t,1} = \boldsymbol{E}_1 \times \boldsymbol{n}_{1\to 2}$, and where the fields are evaluated along the interface. Given the linear polarization along $\hat{\boldsymbol{x}}$ of the excited guided modes propagating along the jet, the radiation pressure depends on the azimuth θ.

This implies that, strictly speaking, the jet cross-section is not circular. However, we notice that $\Pi = \varepsilon_0(n_1^2 - n_2^2)/4|\boldsymbol{E}_1|^2[1 + O((n_1 - n_2)/n_1)]$ with $n_1 - n_2 \ll n_1$ and $|\boldsymbol{E}_1|^2 \simeq |\sum_m \boldsymbol{E}_\perp^{(m)}|^2 (r = R_1)$, which is independent of θ. Consequently, the azimuthal dependence of Π can be safely neglected in the weakly guiding regime.

When the propagation is multi-modal, interferences between the propagating guided modes, which have different propagation constants, may lead to a z-dependent radiation pressure. This would break the z-invariance assumption. However, the experiments reported in Brasselet *et al.* (2008), although corresponding to the multi-mode regime, were successfully described by neglecting such possible interference effects. Therefore, discarding the interferences between the modes, i.e. writing $|\sum_m \boldsymbol{E}_\perp^{(m)}|^2 = \sum_m |\boldsymbol{E}_\perp^{(m)}|^2$, we have (Brasselet & Delville 2008):

$$\Pi = \mathscr{P}\frac{4(n_1 - n_2)}{\pi^2 w_0^2 R_1^4 c}\sum_m \left[\frac{J_1^2(\kappa_m R_1)}{J_0^2(\kappa_m R_1)} + \frac{K_1^2(\gamma_m R_1)}{K_0^2(\gamma_m R_1)}\right]^{-2} \left|\int_0^\infty \mathscr{R}_m(r)\mathrm{e}^{-r^2/w_0^2} 2\pi r \,\mathrm{d}r\right|^2. \quad (5.5)$$

Nevertheless, as justified in the next subsection, our experiments correspond to the monomodal propagation of light and weakly guiding approximation. This validates the use of (5.5).

An experimental jet radius is a mechanically stable solution of (4.11) using (5.5), i.e. a root of (4.11), labelled as $R_{1,eq}$, for which

$$\left.\frac{\partial \Pi}{\partial R_1}\right|_{\mathscr{P}} (R_1 = R_{1,eq}) < \left.\frac{\partial}{\partial R_1}\left(\frac{\sigma}{R_1}\right)\right|_{\mathscr{P}} (R_1 = R_{1,eq}) = -\frac{\sigma}{R_{1,eq}^2}. \quad (5.6)$$

The solutions of (4.11) that correspond to our experiments are plotted in figure 5(*b–g*), where black and grey curves refer to stable and unstable solutions, respectively.

Notice that the condition of mechanical stability of the jet against any homogeneous fluctuation of R_1 all along the jet (5.6) implies stability against varicose shape perturbation of any wavenumber q_v, i.e. the suppression of the Rayleigh–Plateau instability. This can be shown by considering the simplified problem of the stability of a liquid jet with free surface and inviscid dynamics, and by following the linear stability analysis performed by Marr-Lyon *et al.* (2001). For this purpose, let us consider infinitesimal sinusoidal disturbances of R_1, $\delta R_1(z)$, and of pressure of the phase 1, δp_1, with wavenumber q_v. In addition, we assume the corresponding variation of the guided electromagnetic field along the deformed jet to be adiabatic (i.e. power-preserving). Then the linearization of (4.9) with $p_2 = p_0$ and $\eta_1 = \eta_2 = 0$ leads to $\delta p_1 = \Upsilon(q_v)\delta R_1$ with $\Upsilon(q_v) = -\sigma/R_{1,eq}^2 - \partial\Pi/\partial R_1|_{\mathscr{P}}(R_{1,eq}) + \sigma q_v^2$. Since the condition (5.6) for optical stabilization of a jet corresponds to $\Upsilon(0) > 0$, and since $\Upsilon(q_v) > \Upsilon(0)$ $\forall q_v > 0$, one has $\Upsilon(q_v) > 0$ $\forall q_v > 0$. This inequality means that a pressure difference builds up between the bulges and the constrictions of the jet. This pressure difference drives a flow that leads to the release of the bulges for any q_v. Consequently, stability against varicose disturbance of any wavenumber is achieved. Considering the complete problem of two phases with finite viscosities does not alter this conclusion (Johns & Narayanan 2002). Noticeably, the jet formation mechanism employed here intrinsically ensures its overall stability against varicose perturbations.

5.2. *Comparison between model and experiment*

As shown in figure 5(*b–g*), the jet diameter d is typically single-valued at low power whereas it is multi-valued at high power. These predictions are compared with the experimental diameter of part B of the observed dripping jets as a function of the incident beam power $\mathscr{P}$ for the same temperatures; see the open circles in figure 5(*b–g*).

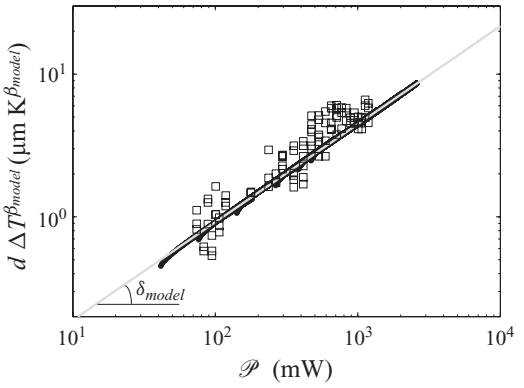

FIGURE 6. Global representation of the variations of the jet diameter d versus $\mathscr{P}$ and ΔT. Solid black curves: predicted variations of $d\ \Delta T^{\beta_{model}}$, $\beta_{model} = 0.85$ versus $\mathscr{P}$ restricted to the first stable branches only for $\Delta T = 1$, 2, 4, 8, 12 and 15 K and $w_0 = 3.47$ μm. Solid grey curve: best power-law fit suggesting an empirical scaling law $d \sim \Delta T^{-\beta_{model}} \mathscr{P}^{\delta_{model}}$, $\delta_{model} = 0.69$. Open symbols: measured variations of $d\ \Delta T^{\beta_{model}}$ versus $\mathscr{P}$.

Although the overall behaviour of the measured diameters is more noisy than in the case of liquid bridges (Brasselet *et al.* 2008), the experimental data clearly correspond to the stable branch of smallest diameters (hereafter called the 'first stable branch'). This is true even in the range of $\mathscr{P}$ for which $d(\mathscr{P})$ is predicted to be multi-stable, as in figure 5(*d*, *g*). We believe that the observed noisy data could be attributed to the feedback of the hydrodynamics associated with the jet unsteadiness (part C of the jet) on the jet diameter. For this reason, the following procedure has been adopted for evaluation of the overall agreement between theory and experiment.

First, we retain the first stable branch of $d(\mathscr{P})$ for each temperature and fit them with an empirical power law of the form $A_{model} \Delta T^{-\beta_{model}} \mathscr{P}^{\delta_{model}}$, where A_{model}, β_{model} and δ_{model} are the adjustable parameters. The best fit corresponds to $\beta_{model} = 0.85$ and $\delta_{model} = 0.69$. Then, the experimental and theoretical quantities $d\ \Delta T^{\beta_{model}}$ are plotted versus $\mathscr{P}$, as shown in figure 6, where the grey curve refers to the best power-law fit. An overall satisfactory agreement between experiment and model is found.

This demonstrates that the diameter of part B of the jet actually obeys a model of cylindrical step-index optical waveguide of circular cross-section and whose diameter is solely determined by the radiation pressure of the guided beam propagating along it. The scattering force density field and the flow can now be determined from the knowledge of the electromagnetic field distribution inferred by the light propagation model.

6. Model of flow induced by the scattering force density

6.1. *Boundary conditions and flow rate constraint*

The flow in phases 1 and 2 is obtained by solving (4.3), which requires four independent constraints since we are dealing with a set of two second-order differential equations. These constraints are determined from the following considerations.

(i) Continuity of the tangential velocity at the interface,

$$v_{z,1}(r = R_1) = v_{z,2}(r = R_1). \tag{6.1}$$

(ii) Continuity of the shear stress at the interface, which is given by (4.10).

(iii) No-slip condition at the cell sidewalls. Since the horizontal cross-section of the sample cell is rectangular, this condition is incompatible with a velocity field of cylindrical symmetry. However, as said in § 3, a suitable observation of the jet is done by forming it close to a side window, typically $\sim 50\,\mu\mathrm{m}$. Therefore, we introduce an effective outer radius R_2 at which a no-slip boundary condition of cylindrical symmetry can be imposed on the flow,

$$v_{z,2}(r = R_2) = 0. \tag{6.2}$$

It should be kept in mind that the value of such an effective outer radius R_2 of the flow may range from $50\,\mu\mathrm{m}$ up to the typical dimension of the horizontal cross-section of the cell, i.e. 1 cm. Moreover, this value can not be deduced from experimental considerations. However, it is well known that the dependence on the outer diameter of the flow characteristics has a logarithmic behaviour and can therefore be neglected (Thouvenel-Romans, van Saarloos & Steinbock 2004).

(iv) The last constraint is found by noting that the net axial flow of the outer fluid, Q_2, is zero,

$$Q_2 = \int_{R_1}^{R_2} 2\pi r v_{z,2}(r)\ \mathrm{d}r = 0. \tag{6.3}$$

We notice that, since the droplets emitted by the jet tip first sink into the lower phase as they are transported by the bulk flow and then rise up to the interface by buoyancy, the net flow of the inner fluid is zero too. However, the net flow rate Q_1 of the inner fluid across any cross-section of the jet,

$$Q_1 = \int_0^{R_1} v_{z,1}(r) 2\pi r\ \mathrm{d}r, \tag{6.4}$$

is non-zero and its value corresponds to the mean dripping flow rate.

6.2. *Exact determination of the flow*

To ease the determination of the flow, the corresponding equations are made dimensionless owing to the following procedure, which consists in the introduction of characteristic length, scattering force densities, velocity and axial pressure gradient.

(i) The jet radius R_1 is chosen as the characteristic length scale and we define the reduced length $\tilde{r} = r/R_1$ and wavenumbers $\tilde{\kappa} = \kappa_1 R_1$ and $\tilde{\gamma} = \gamma_1 R_1$.

(ii) The scattering force density in each phase is written as $\boldsymbol{f}_1^{scatt} = F_1 J_0^2(\tilde{\kappa}\tilde{r})\hat{\boldsymbol{z}}$ and $\boldsymbol{f}_2^{scatt} = F_2 K_0^2(\tilde{\gamma}\tilde{r})\hat{\boldsymbol{z}}$, where $F_{1,2}$ are obtained combining (4.6), (5.1) and (5.2).

(iii) The characteristic velocity is chosen as the Poiseuille characteristic velocity in phase 1, $\eta_1/F_1R_1^2$, and we define the reduced velocities $\tilde{v}_{z,i} = \eta_1 v_{z,i}/F_1 R_1^2$ $(i = 1, 2)$.

(iv) The characteristic axial pressure gradient is chosen as the scattering force density in the phase 1, F_1, and we define the reduced axial pressure gradient $\psi = C/F_1$.

On the one hand the velocity field in phase 1 is obtained by solving (4.3) with $i = 1$ (omitting the tildes in the following),

$$\frac{\partial}{\partial r}\left(r\frac{\partial v_{z,1}}{\partial r}\right) = \psi r - r J_0^2(\kappa r). \tag{6.5}$$

Since the velocity is finite on the axis, its solution is

$$v_{z,1} = \frac{\psi}{4}\left(r^2 - r_1^2\right) - \frac{1}{4}\left\{r^2\left[J_0^2(\kappa r) + 2J_1^2(\kappa r) - J_0(\kappa r)J_2(\kappa r)\right]\right.$$
$$\left. - r_1^2\left[J_0^2(\kappa r_1) + 2J_1^2(\kappa r_1) - J_0(\kappa r_1)J_2(\kappa r_1)\right]\right\}, \tag{6.6}$$

where r_1 is an integration constant. On the other hand, the velocity field in phase 2 is obtained by solving (4.3) with $i=2$,

$$\frac{\partial}{\partial r}\left(r\frac{\partial v_{z,2}}{\partial r}\right)=\psi\mu r-\mu\zeta r K_0^2(\gamma r), \tag{6.7}$$

where $\mu=\eta_1/\eta_2$ and $\zeta=F_2/F_1$. Its solution is

$$\begin{aligned} v_{z,2}=&\frac{\psi\mu}{2}\left[\frac{1}{2}(r^2-r_1'^2)-r_0'^2\ln\left(|r/r_1'|\right)\right]\\ &-\frac{\mu\zeta}{2}\left\{-r_0'^2\left(K_0^2(\gamma r_0')-K_1^2(\gamma r_0')\right)\ln\left(|r/r_1'|\right)+\frac{1}{2}\left[r^2\left(K_0^2(\gamma r)-2K_1^2(\gamma r)\right.\right.\right.\\ &\left.\left.\left.+K_0(\gamma r)K_2(\gamma r)\right)-r_1'^2\left(K_0^2(\gamma r_1')-2K_1^2(\gamma r_1')+K_0(\gamma r_1')K_2(\gamma r_1')\right)\right]\right\}, \end{aligned} \tag{6.8}$$

where r_0', r_1' are two additional integration constants.

The four unknown constants ψ, r_1, r_0' and r_1' are determined by the set of four coupled nonlinear equations that result from the three boundary conditions and the zero mean outer flow constraint. Indeed, (6.1), (4.10), (6.2) and (6.3) can be, respectively, expressed as

$$\begin{aligned} 0=&\frac{\psi}{4}\left(1-r_1^2\right)-\frac{1}{4}\left[J_0^2(\kappa)+2J_1^2(\kappa)-J_0(\kappa)J_2(\kappa)-r_1^2\left(J_0^2(\kappa r_1)+2J_1^2(\kappa r_1)\right.\right.\\ &\left.\left.-J_0(\kappa r_1)J_2(\kappa r_1)\right)\right]-\frac{\psi\mu}{2}\left[\frac{1}{2}\left(1-r_1'^2\right)+r_0'^2\ln(|r_1'|)\right]+\frac{\mu\zeta}{2}\left\{r_0'^2\left(K_0^2(\gamma r_0')\right.\right.\\ &\left.\left.-K_1^2(\gamma r_0')\right)\ln(|r_1'|)\frac{1}{2}\left[K_0^2(\gamma)-2K_1^2(\gamma)+K_0(\gamma)K_2(\gamma)-r_1'^2\left(K_0^2(\gamma r_1')\right.\right.\right.\\ &\left.\left.\left.-2K_1^2(\gamma r_1')+K_0(\gamma r_1')K_2(\gamma r_1')\right)\right]\right\}, \end{aligned} \tag{6.9}$$

$$0=\psi r_0'^2-\left[J_0^2(\kappa)+J_1^2(\kappa)\right]+\zeta\left[K_0^2(\gamma)-K_1^2(\gamma)-r_0'^2\left(K_0^2(\gamma r_0')-K_1^2(\gamma r_0')\right)\right], \tag{6.10}$$

$$\begin{aligned} 0=&\psi\left[\tfrac{1}{2}\left(\rho^2-r_1'^2\right)-r_0'^2\ln(|\rho/r_1'|)\right]-\zeta\left\{-r_0'^2\left(K_0^2(\gamma r_0')-K_1^2(\gamma r_0')\right)\ln(|\rho/r_1'|)\right.\\ &+\tfrac{1}{2}\left[\rho^2\left(K_0^2(\gamma\rho)-2K_1^2(\gamma\rho)+K_0(\gamma\rho)K_2(\gamma\rho)\right)\right.\\ &\left.\left.-r_1'^2\left(K_0^2(\gamma r_1')-2K_1^2(\gamma r_1')+K_0(\gamma r_1')K_2(\gamma r_1')\right)\right]\right\}, \end{aligned} \tag{6.11}$$

$$\begin{aligned} 0=&\psi\left\{\frac{1}{4}(\rho^4-1)-\frac{r_1'^2}{2}(\rho^2-1)-r_0'\left[\rho^2\ln\left(|\rho/r_1'|\right)\ln(|r_1'|)-\frac{1}{2}(\rho^2-1)\right]\right\}\\ &+\zeta r_0'^2\left(K_0^2(\gamma r_0')-K_1(\gamma r_0')\right)\left[\rho^2\ln(|\rho/r_1'|)+\ln(|r_1'|)-\frac{1}{2}(\rho^2-1)\right]\\ &-\zeta(I_1+I_2-2I_3)+\frac{\zeta}{2}r_1'^2\left(K_0^2(\gamma r_1')-2K_1^2(\gamma r_1')+K_0(\gamma r_1')K_2(\gamma r_1')\right)(\rho^2-1), \end{aligned} \tag{6.12}$$

where $\rho=R_2/R_1$, $I_1=\int_1^\rho r^3K_0^2(\gamma r)\,\mathrm{d}r$, $I_2=\int_1^\rho r^3K_0(\gamma r)K_2(\gamma r)\,\mathrm{d}r$, $I_3=\int_1^\rho K_1^2(\gamma r)\,\mathrm{d}r$.

6.3. *Numerical resolution of (6.9)–(6.12)*

The system of four coupled nonlinear equations (6.9)–(6.12) is solved numerically for each of the experimentally investigated temperatures, for $w_0=3.47\,\mu\mathrm{m}$, $R_2/R_1=50$ and a range of power that corresponds to the first stable branch for the jet

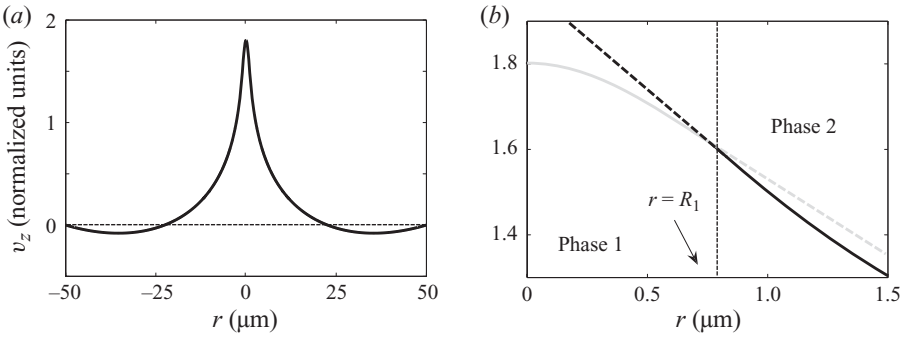

FIGURE 7. Dimensionless velocity profile computed for $\Delta T = 15\,\mathrm{K}$, $\mathscr{P} = 1\,\mathrm{W}$, $w_0 = 3.47\,\mu\mathrm{m}$, and effective cell diameter $R_2 = 50R_1$. (*a*) Overall profile. (*b*) Close-up of the vicinity of the jet axis. The continuity of the shear stress at the interface is satisfied through the slope jump of the velocity profile at $r = R_1$ from phase 1 (grey solid curve in phase 1, extended as a dashed grey straight line in phase 2 as a guide for the eye) to phase 2 (black solid curve in phase 2, extended as a dashed black straight line in phase 1) due to the viscosity contrast between phases 1 and 2.

diameter, according to the following procedure. We first introduce the vector of unknowns $\boldsymbol{x} = (\psi, r_1, r_0', r_1')$ and rewrite (6.9)–(6.12) as $\boldsymbol{F}(\boldsymbol{x}) = \boldsymbol{0}$. The zeros of $\boldsymbol{F}$ are then found using a standard Newton–Raphson method, which is an efficient way to obtain solutions in the investigated range of parameters. The accuracy of the results is such that $Q_2 = 0$ up to a 10^{-8} relative error with respect to Q_1, namely $Q_2/Q_1 < 10^{-8}$ is always satisfied. Notice that, although the dimensionless flow is explicitly independent of $\mathscr{P}$ and of w_0, it actually depends on these quantities through the jet radius $R_1(\mathscr{P}, T, w_0)$. For ease of numerical implementation of (6.9)–(6.12) we chose $R_2/R_1 = 50$. Given the range of experimental variations of R_1, this corresponds to $R_2 > 50\,\mu\mathrm{m}$, i.e. to a realistic value for R_2, see § 6.1. We checked that, as expected (Thouvenel-Romans *et al.* 2004), the dependence of Q_1 on R_2 is logarithmic in the $R_2/R_1 \gg 1$ limit.

6.4. *Predicted velocity profiles and flow rate*

A typical dimensionless velocity profile computed according to this model is displayed in figure 7 for $\Delta T = 15\,\mathrm{K}$ and $\mathscr{P} = 1\,\mathrm{W}$. The constraint of zero mean flow in phase 2 results in a counter flow in phase 2 away from the beam. The velocity actually vanishes at the outer flow boundary. The continuity of the velocity and of the shear stress at the interface is satisfied, as shown in figure 7(*b*), through respectively the continuity of the velocity profile at $r = R_1$ and its slope jump from phase 1 (grey solid curve) to phase 2 (black solid curve) due to the viscosity contrast between phases 1 and 2.

Once the flow has been determined, the associated jetting flow rate Q_1 is computed using as input parameter for (6.6) only the first stable branch of solution for $R_1(\mathscr{P})$ given by the optical liquid fibre model discussed in § 5. The predicted variations of Q_1 versus $\mathscr{P}$ for $T - T_c = 1, 2, 4, 8, 12$ and $15\,\mathrm{K}$ and $w_0 = 3.47\,\mu\mathrm{m}$ are shown in figure 8. As expected, since only the first stable branch of $R_1(\mathscr{P})$ has been considered, Q_1 is a continuous and increasing function of $\mathscr{P}$. For the experimentally investigated ranges of $\mathscr{P}$, Q_1 is predicted to vary between 2×10^1 and $5 \times 10^2\,\mu\mathrm{m}^3\,\mathrm{s}^{-1}$.

The model can now be compared to the experimental measurements of Q_1.

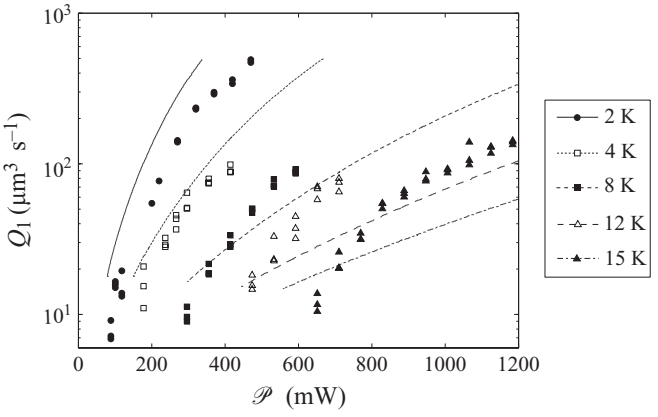

FIGURE 8. Curves: calculated dripping flow rate Q_1 as a function of $\mathscr{P}$ for each of the experimentally investigated temperatures that corresponds to the first stable branch of $R_1(\mathscr{P})$ only (see figure 5). Symbols: experimental data.

7. Flow rate measurements and their comparison with the model

7.1. *Principle of the flow measurements*

Once a steadily emitting jet has been established, a movie of its dripping tip is acquired using a CCD video camera working at 25 fps. A typical series of pictures is shown in figure 9(*a–d*). The size of the emitted droplets is always comparable to the jet diameter. Their ellipsoidal shape is due to the stretching action of the radiation pressure of the beam emerging from the jet (Zhang & Chang 1988). Once emitted, despite buoyancy, a droplet is transported downwards by the bulk flow and by the scattering force exerted on it.

In agreement with the observations, we find that the amplitude Δu of the relative velocity of a drop with respect to the surrounding continuous phase that results from the balance of buoyancy and Stokes drag, $-\Delta u\,\hat{z}$, is much smaller than the amplitude u of the observed sinking velocity of the drop transported by the light scattering induced flow, $u\,\hat{z}$. Indeed, considering spherical droplets of radius R, we have $\Delta u \simeq (2/9)(\rho_2 - \rho_1)gR^2/\eta_2$, where g is the acceleration of gravity. This gives $\Delta u \simeq 3\,\mu\mathrm{m\,s^{-1}}$ for $\Delta T = 2\,\mathrm{K}$ and $R = 5\,\mu\mathrm{m}$, whereas $U \simeq 75\,\mu\mathrm{m}\cdot\mathrm{s}^{-1}$ (see figure 9).

Quantitatively, a given video sequence is analysed in the following way. Whenever a droplet is emitted, its volume V is measured by fitting its shape to an ellipse of major axis a and minor axis b (see figure 9*e*), namely $V = (4/3)\pi ab^2$. A histogram of the droplet volumes measured over a 250 s duration is shown in figure 9(*f*), showing a rather broad distribution. Thus Q_1 is defined as the total volume of a few tens of droplets divided by the corresponding duration of time.

Notice that the value of the Reynolds number computed using w_0 as the characteristic diameter of the jet and the measured velocity u is $Re \simeq 3 \times 10^{-4}$. This justifies *a posteriori* the assumption of creeping flow made throughout the model.

7.2. *Comparison with the model*

In figure 8, the variation in the measured dripping flow rate Q_1 versus $\mathscr{P}$ is superimposed on their prediction using the first stable branches of the $R_1(\mathscr{P})$ laws as the input jet geometry. Satisfactory overall agreement between experiments and the model is observed, regarding both trends and orders of magnitudes. However, we

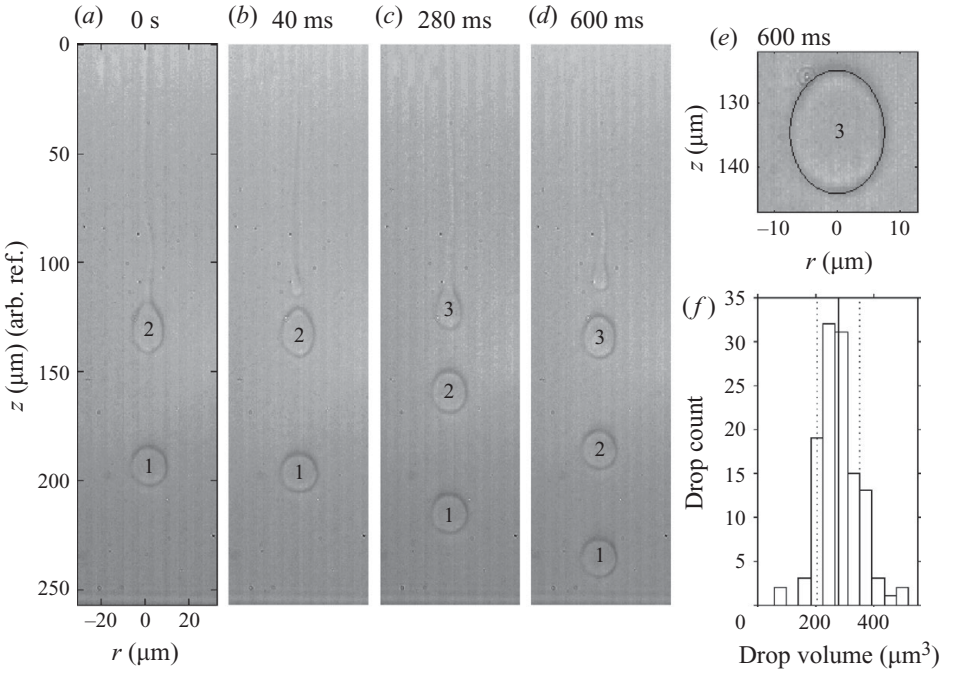

FIGURE 9. (*a–d*) Series of pictures of the dripping jet tip at $\Delta T = 2\,\mathrm{K}$, $\mathscr{P} = 320\,\mathrm{mW}$, $w_0 = 3.47\,\mu\mathrm{m}$ taken at (*a*) 0 s, (*b*) 40 ms, (*c*) 280 ms and (*d*) 600 ms. (*e*) Zoom of picture (*d*) showing the superimposed best elliptic fit of droplet 3 used to determine its volume. (*f*) Histogram of the drop volumes measured over a 250 s duration at $T - T_c = 2\,\mathrm{K}$, $\mathscr{P} = 200\,\mathrm{mW}$, $w_0 = 3.47\,\mu\mathrm{m}$. Solid vertical line (resp. dashed vertical lines) marks the mean value, 278 μm, (resp. the standard deviation, 75 μm) of the volume distribution.

notice that flow rates are theoretically overestimated at small ΔT and underestimated at large ΔT. In particular, we notice steeper than predicted variations of Q_1 at low $\mathscr{P}$, especially at $\Delta T = 15\,\mathrm{K}$. We attribute this behaviour to the increasing relative importance of buoyancy compared to the scattering force as a function of ΔT. In fact, we experimentally observed that buoyancy impedes the detachment of the droplets and their advection by the bulk flow for the larger values of ΔT.

As was done for the jet diameter study, a global representation is useful in order to gauge the overall compatibility between the model and the experimental data. For this purpose, the theoretical $Q_1(\mathscr{P})$ curves shown in figure 8 have been fitted using an empirical power law of the form $A_{model}\,\Delta T^{-\beta_{model}}\,\mathscr{P}^{\delta_{model}}$, where A_{model}, β_{model} and δ_{model} are adjustable parameters. The best fit gives $\beta_{model} = 2.44$ and $\delta_{model} = 2.28$. The quantity $Q_1\ \Delta T^{\beta_{model}}$ versus $\mathscr{P}$ is then plotted for both the predicted and measured flow rates in figure 10, where the grey curve corresponds to the best power-law fit of the model. Such a comparison between experimental and theoretical scaling behaviours calls for four remarks.

(i) The overall agreement between experiment and model is satisfactory regarding trends and orders of magnitudes. This demonstrates the relevance of the model.

(ii) Both the predicted and measured dripping flow rates can be accurately described by a scaling law for the variables $\mathscr{P}$ and ΔT.

(iii) The measured flow rates are shown to obey a power law in $\mathscr{P}$ with an exponent that is larger than its predicted value. This observation is confirmed by the values of the exponents $\beta_{exp} = 1.97$ and $\delta_{exp} = 2.64$ of the best power-law fit of the form

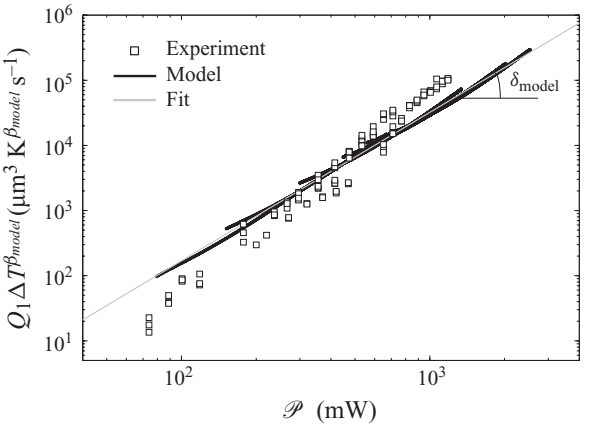

FIGURE 10. Global representation of the predicted and measured dripping flow rate Q_1 versus ΔT and $\mathscr{P}$. Solid black curves: the predicted quantity $Q_1\ \Delta T^{\beta_{model}}$, $\beta_{model} = 2.44$ versus $\mathscr{P}$. Solid grey line: best power-law fit suggesting an empirical scaling law satisfied by the model $Q_1 \propto \Delta T^{\beta_{model}} \mathscr{P}^{\delta_{model}}$, $\delta_{model} = 2.28$. Symbols: measured $Q_1\ \Delta T^{\beta_{model}}$ versus $\mathscr{P}$.

$A_{exp} \Delta T^{-\beta_{exp}} \mathscr{P}^{\delta_{exp}}$ of the whole set of experimental data, which are found to differ from β_{model} and δ_{model} by 21 and 15 %, respectively.

(iv) The experimental data $Q_1\ \Delta T^{\beta_{model}}$ versus $\mathscr{P}$ is strikingly less noisy than the data $d\ \Delta T^{\beta_{model}}$ versus $\mathscr{P}$ shown in figure 6. This demonstrates that Q_1, which is the result of a large-scale flow and is defined as a time-averaged quantity, is weakly sensitive to the spatiotemporal fluctuations of d along the jet.

7.3. *Discussion*

The observed (resp. predicted) nonlinear dependence of Q_1 versus the light power $\mathscr{P}$, $Q_1 \propto \mathscr{P}^{2.64}$ (resp. $Q_1 \propto \mathscr{P}^{2.28}$) is unusual for creeping flows, in particular considering the apparent analogy between this flow and a Poiseuille flow. This is especially true when comparing our situation with a Poiseuille flow in a tube of fixed diameter with liquid walls (Thouvenel-Romans *et al.* 2004). This observed genuine behaviour is reminiscent of the power dependence of the tube diameter. Recalling that the Poiseuille flow rate is proportional to the fourth power of the tube radius and that we found $R_1 \propto \mathscr{P}^{0.69}$, one would expect $Q_1 \propto R_1^4 \mathscr{P} \propto \mathscr{P}^{3.76}$. Such a naive scaling law obviously differs from the observed and predicted ones. This is is due to the combination of several effects. First, the driving force density field is inhomogeneous (as opposed to the homogeneous pressure gradient driving the usual Poiseuille flow). Moreover, the latter depends on the tube radius, which is self-adapted from the total power of the guided light field.

We now analyse the possible reasons for the noticeable differences between the absolute values of the measured and predicted flow rates and by the 21 % (resp. 15 %) difference between β_{model} and β_{exp} (resp. between γ_{model} and γ_{exp}).

(i) The quantitative agreement between the measured and predicted jet diameters validates the use of the theoretical law $R_1(\mathscr{P}, \Delta T, w_0)$ as an input for the flow model. As predicted by Poiseuille's law, Q_1 is expected to depend in a power-law manner on R_1 with an exponent close to 4. Therefore, a given discrepancy between the theoretical and experimental $R_1(\mathscr{P})$ laws may result in a larger one for $Q_1(\mathscr{P})$ laws.

(ii) It is well known that gravity effects are important near second-order transitions. Near the critical consolute line of the microemulsion, the distribution of droplets is expected to become noticeably inhomogeneous in each phase as a result of barodiffusion, i.e. the balance of sedimentation and diffusion. Since we use a microemulsion in the two-phase regime, the balance of the chemical potentials of the two phases at the interface implies that, in the vicinity of the interface, the thermophysical properties of each phase are close to their equilibrium value encountered in a homogeneous two-phase sample in the absence of gravity. Applying to the microemulsion the model of barodiffusion developed for liquid binary mixtures, we can express the steady-state gravity-induced vertical gradient of volume fraction of droplets as $\mathrm{d}\Phi/\mathrm{d}z = \rho_{drop}^2(\rho_{cont}^{-1} - \rho_{drop}^{-1})\chi_T^- g$, where g is the acceleration of gravity (Kumar, Krishnamurty & Gopal 1983). Although $\mathrm{d}\Phi/\mathrm{d}z$ diverges at T_c, the relative variation of Φ over the typical length $L \simeq 200\,\mu\mathrm{m}$ of the jet, $L(\mathrm{d}\Phi/\mathrm{d}z)/\Phi_c$, ranges from 0.02 % for $\Delta T = 15\,\mathrm{K}$ to 0.2 % for $\Delta T = 2\,\mathrm{K}$. Thus, gravity-induced droplet stratification over the jet length can be neglected.

(iii) Electrostriction, thermodiffusion and absorption are known to be responsible for the formation of transverse refractive index and turbidity gradients (Jean-Jean *et al.* 1989). These phenomena may affect both the light propagation and its coupling with the flow and jet shape. It has been shown that, for the relatively small beam waist used in this study, electrostriction is the leading cause of the transverse variation of the refractive index of the microemulsion (Jean-Jean *et al.* 1988). After a transient of duration of the order of some hundreds of milliseconds (Freysz *et al.* 1994), the refractive index is expected to increase along the beam axis by an amount δn such that (Jean-Jean *et al.* 1989):

$$\delta n \sim \left(\left. \frac{\partial \varepsilon}{\partial \Phi} \right|_T \right)^2 \chi_T \frac{\mathscr{P}}{\pi n^2 c w_0^2}. \tag{7.1}$$

First, we consider the possible modification of the radiation pressure distribution exerted on the jet boundary due to transverse gradients of refractive index. Although $\delta n_i/n_i$ reaches a few per cent in each phase in our case, $\delta n_1 \simeq \delta n_2$ at the jet boundary. Consequently, the effect of electrostriction on the radiation pressure is negligible. Second, it is known that the transverse dependence of δn_i is responsible for beam self-focusing in the same kind of microemulsions (Freysz, Afifi & Ducasse 1985). Self-focusing was reported to be reproducibly observed only when the sample was confined in glass capillaries of 200 μm optical path (Jean-Jean *et al.* 1988). In our case, where a millimetre-scale sample is used, we believe that the existing large scale flows hinders the formation of transverse refractive index gradients driven by droplet diffusion. Finally, Jean-Jean *et al.* (1989) estimated the transverse variation of the turbidity of the microemulsion, $\delta\tau$, to be

$$\delta\tau \sim \left. \frac{\partial \tau}{\partial T} \right|_\Phi \frac{\alpha_{abs}\mathscr{P}}{\pi \Lambda_T}, \tag{7.2}$$

where $\Lambda_T = 0.13\,\mathrm{W\,m^{-1}K^{-1}}$ is the thermal conductivity of the microemulsion. Since $\delta\tau/\tau$ is less than 1 % in our case, its effect on the scattering force density field, hence the bulk flow, can be neglected.

(iv) We notice that the predicted flow rate depends on the radius R_2 of the outer boundary. The influence of R_2 can be retrieved from the analysis of a simple situation where an uniform force density f is exerted on phase 1 only. In that case, $Q_1 \sim (\pi f R_1^4/2\eta_2)\ln(R_2/R_1)$ for $R_2/R_1 \to \infty$ (Thouvenel-Romans *et al.*

2004). Thus, we expect Q_1 to depend on R_2 in a logarithmic manner. In practice, $R_1 \simeq 1\,\mu\text{m}$ and R_2 ranges from $50\,\mu\text{m}$ to $1\,\text{cm}$. Since for ease of numerical implementation we chose $R_2/R_1 = 50$, Q_1 may be underestimated by a factor $\ln(1\,\text{cm}/1\,\mu\text{m})/\ln(50\,\mu\text{m}/1\,\mu\text{m}) \simeq 2.3$ at most. This factor depends on the value of the effective radius of the outer boundary, which is difficult to estimate.

Finally, we stress that, in the present study, the thermophysical properties of the microemulsion in the two-phase region have been estimated using scaling laws that are accurate only asymptotically close to $T = T_C$. This could also explain the observed discrepancies between our model and the experiments. Moreover, we believe that any improvement of the model that would break the z-invariance on which the description of the flow and of the jet relies (for example, by including the effects of gravity or of self-focusing) would be useless given the uncertainties on the thermophysical properties of the microemulsion.

8. Conclusion and opening

In this study, we have reported on the first direct observation of a bulk flow induced by light within a light-scattering fluid. This was done by observing the dripping of a jet induced by the radiation pressure of light. The quantitative experimental analysis was performed by the simultaneous measurement of the liquid jet diameter and the dripping flow rate. We derived a model of light-driven creeping flow underlying the dripping that accounts for the electromagnetic and hydrodynamics features of the phenomenon. The agreement between the measurements and the model was found to be satisfactory. This unambiguously demonstrates that the transfer of linear momentum from light to a fluid through light scattering can drive a flow.

More generally, this mechanism of flow actuation based on the transfer of momentum from a wave to liquids also underlies the well-known acoustic streaming phenomenon, which relates to the steady flows induced by high-intensity acoustic beams in sound-absorbing homogeneous liquids (Nyborg 1997). Of course, the physical processes underlying the transfer of momentum differ from light-scattering to sound-absorbing fluids. In the first case, the light–matter interaction is conservative (elastic light scattering), i.e. without absorption of electromagnetic energy by matter, hence without heating. In the latter case, since sound propagation in a homogeneous fluid basically involves heat conduction and viscous diffusion of momentum, its transfer of momentum (more precisely pseudo-momentum; see McIntyre 1981) to the fluid is dissipative and induces heating. Nevertheless both these mechanisms of momentum transfer result in the same kind of force density fields localized within the beams and driving flows always oriented in the direction of propagation of the beams. The reason why the heating induced in acoustic streaming experiments performed in sound-absorbing homogeneous fluids is sustainable is that the sound velocity is 10^5 times smaller than light velocity. Since the velocity of energy of the wave approximately equals the ratio of the intensity to the momentum of a progressive wave, for the same power attenuation per unit length of a progressive wave, the rate of momentum transfer from the wave to the fluid per unit length is 10^5 larger for sound than for light. Consequently, a noticeable flow purely induced by sound absorption can be observed, whereas light absorption induces several side effects which mask the effect of momentum transfer, for instance thermal convection. Nevertheless, acoustic streaming involving sound scattering as the main cause of beam attenuation is absolutely conceivable (as a matter of fact, the deformation of sound scattering and absorbing, visco-elastic media by intense acoustic beams, that is, the analogue

of streaming flows in fluids, is at the basis of the acoustic radiation pressure imaging technique of biological tissues). This successful description of the light-induced jetting as the result of both the scattering force density and of optical radiation pressure raises the question of a possible combined action of acoustic streaming and acoustic radiation pressure in the triggering of the acoustic fountain phenomenon (Wood & Loomis 1927; Issenmann *et al.* 2008; Tan, Friend & Yeo 2009). Notice finally that the same side effects as for light-scattering-induced flows, i.e. the longitudinal and axial segregation of the scattering particles, are commonly used for acoustically concentrating, sorting and sizing microparticles (Kuznetsova & Coakley 2004) and for achieving ultrasonic four-wave mixing in suspensions (Simpson & Marston 1995).

Appendix A. Thermophysical properties of the microemulsion

A.1. *Osmotic susceptibility*

The osmotic susceptibility χ_T of a binary mixture is usually determined from the measurement of its turbidity τ (i.e. the relative loss of intensity per unit propagation length of a light wave propagating through the fluid due to light scattering) using:

$$\tau = \frac{\pi^3}{\lambda_0^4}\left(\left.\frac{\partial\varepsilon}{\partial\Phi}\right|_T\right)^2 k_B T \chi_T \left(\frac{2\alpha^2+2\alpha+1}{\alpha^3}\ln(1+2\alpha) - 2\frac{1+\alpha}{\alpha^2}\right), \qquad (A\,1)$$

where $\alpha = 2(k\xi)^2$, $k = 2\pi n/\lambda_0$, λ_0 is the wavelength in vacuum of the incident light, ξ the correlation length of the composition fluctuations within the binary mixture (Ornstein & Zernike 1914; Puglielli & Ford 1970). (A 1) was historically first applied to near-critical pure fluids (for pure fluids, Φ is replaced by the density ρ, which is the order parameter of the liquid–gas phase transition). Puglielli & Ford (1970) found their determination of the susceptibility in near-critical SF_6 from their turbidity measurements in quantitative agreement with previous measurements using other techniques, validating (A 1) for pure fluids. Validation of (A 1) in several binary mixtures was also performed, e.g. in the near-critical methanol-cyclohexane binary mixture by Jacobs (1986).

Freysz (1990) measured the turbidity τ at three different wavelengths $\lambda_0 = 647.1$, 530.9 and 476.2 nm of a one-phase near-critical microemulsion of composition (mass fraction of toluene 71.4 %, of water 8.5 %, of sodium dodecyl sulphate 3.95 % and of n-butanol 16.15 %) very close to the composition of the sample we used for our study, in particular with the same water/SDS mass ratio, which determines the droplet size. His measurements are reproduced in figure 11. Although the best fits of his turbidity measurements by (A 1) demonstrated its applicability to near-critical microemulsions, the amplitude χ_{T0}^+ of the critical scaling law (2.1) for χ_T in the one-phase region was unfortunately not explicitly given.

In order to determine χ_{T0}^+, we fitted his turbidity measurements at each investigated wavelength using (A 1) and the asymptotic critical scaling laws (2.2) and (2.1), the fitting parameters given in Freysz (1990) and reproduced in table 1, $n = 1.464$, $\gamma = 1.24 = (2-\eta)\nu$, $\eta = 0.03$ and $\partial n/\partial\Phi|_T = -0,11$ (Jean-Jean 1987). The best fits, shown in figure 11, accurately describe the three experimental data sets. In the inset of figure 11 we have plotted the variations of $\tau(|\Delta T|/T_c)^\gamma/\tau_{exp}$ as a function of $-\Delta T = T_c - T$. This quantity is expected to be constant and equal to χ_{T0}^+ when χ_T actually obeys the asymptotic critical scaling law (2.1), i.e. sufficiently close to T_c. We observe that this quantity is indeed constant close to T_c and takes close values for the three investigated wavelengths. We deduce $\chi_{T0}^+ = 5.78\ 10^{-6}\,\mathrm{Pa}^{-1}$ with a 10 % accuracy

λ_0 (nm)	647.1	530.9	476.2
ξ_0^+ (Å)	44.2	38.4	42.5
T_c (°C)	34.3	34.2	34.0

TABLE 1. Values of the parameters used for fitting the turbidity measurements of Freysz (1990).

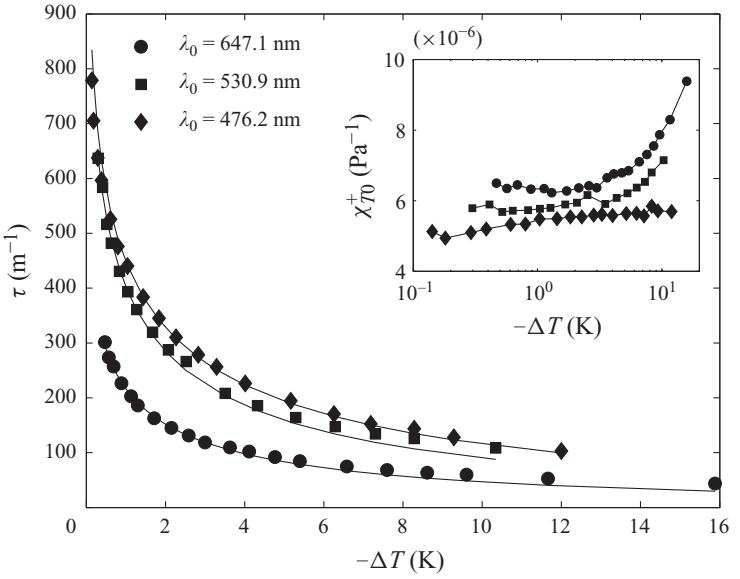

FIGURE 11. Turbidity of the one-phase microemulsion as function of the distance to its critical temperature for three optical wavelengths. Inset: variations of $\tau(|\Delta T|/T_c)^\gamma/\tau_{exp}$ as function of of the distance to its critical temperature, which close to T_c identifies with the amplitude χ_{T0}^+ of the critical scaling law (2.1) for the osmotic suceptibility χ_T.

(see table 1 and figure 11). The numerical value of the universal amplitude ratio $\xi_0^+(\Delta\Phi_0/2)^{2/3}(k_B T_c \chi_{T0}^+)^{-1/3}$ calculated using this value of χ_{T0}^+ and the above given values of ξ_0^+ and $\Delta\Phi_0$ is 0.53, in close agreement with its average value 0.66 ± 0.1 for binary mixtures (Beysens *et al.* 1982).

A.2. *Viscosity*

Freysz (1990) also measured the temperature dependence of the dynamic viscosity η of a near-critical one-phase microemulsion sample of volume fraction of droplets $\Phi = 0.13$ slightly larger than our sample ($\Phi = 0.11$) in the temperature range 22.5–30 °C. He fitted his measurements using the following linear law:

$$\eta(\Phi = 0.13, T) = (1.934 - 0.019(T - 273.15)) \cdot 10^{-3} \text{ Pa s.} \qquad \text{(A 2)}$$

In order to deduce the viscosity of each phase of our two-phase near-critical microemulsion at every temperature, we have to choose the most accurate law describing the dependence of the viscosity of the microemulsion on the volume fraction of droplets. For very dilute suspensions of solid spheres ($\Phi < 0.03$), Einstein's law $\eta_{Einstein} = \eta_{cont}(1 + 2.5\Phi)$, where η_{cont} is the dynamic viscosity of the continuous phase, is known to be accurate. For higher-volume fractions, it is necessary to add to Einstein's law a quadratic correction: $\eta_{Batchelor} = \eta_{Einstein} + 6.2\Phi^2$ (Batchelor's law).

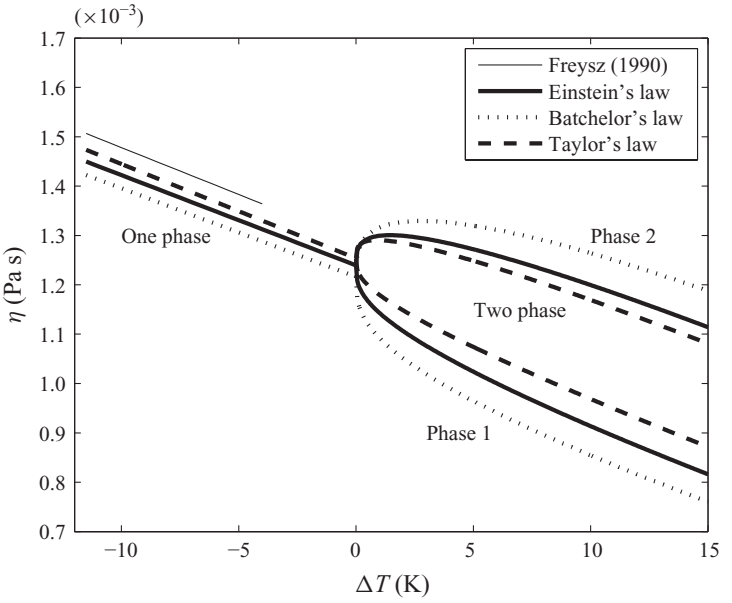

FIGURE 12. Measured and extrapolated temperature dependence of the viscosity of the microemulsion in the one-phase and two-phase regimes.

For a very diluted suspension of liquid droplets of viscosity η_d, Taylor established: $\eta_{Taylor} = \eta_{cont}(1 + ((\eta_{cont} + 2,5\eta_d)/(\eta_{cont} + \eta_d))\Phi)$. For very diluted suspensions of droplets stabilized by surfactants covering their interface with the continuous phase (emulsions), a law has been proposed by Danov (2001) involving all the interfacial viscoelastic properties of the surfactant, which are hard to gather. On the other hand, considering the relatively large volume fractions concerned in this study, we would need a law for emulsions presenting at least a quadratic correction in Φ. In the absence of such a law, we can compare the predictions of Einstein's, Batchelor's and Taylor's laws.

First, we infer the temperature dependence of the viscosity of the continuous phase η_{cont} in the two-phase region ($T > T_c$) by extrapolating the empirical viscosity law (A 2). The extrapolation is model-dependent:

$$\eta_{cont}(T) = \frac{\eta(\Phi = 0.13, T)}{1 + 2.5 \times 0.13} \text{ using Einstein's law,} \tag{A 3}$$

$$\eta_{cont}(T) = \frac{\eta(\Phi = 0.13, T)}{1 + 2.5 \times 0.13 + 6.2 \times 0.13^2} \text{ using Batchelor's law,} \tag{A 4}$$

$$\eta_{cont}(T) = \frac{\eta(\Phi = 0.13, T)}{1 + \dfrac{\eta_{cont}(T) + 2,5\eta_d(T)}{\eta_{cont}(T) + \eta_d(T)} \times 0.13} \text{ using Taylor's law.} \tag{A 5}$$

Since the droplets in the microemulsion are principally composed of water, we solve (A 5) by using for η_d the tabulated temperature dependence of the viscosity of water $\eta_{water} = \exp(5.5263.10^5 T^{-2} - 1685.3T^{-1} - 7.5881)$ (T in K) valid in the temperature domain 20–50°C (Weast 1971). Then, we determine the viscosity of the microemulsion using the three laws and (2.3). The resulting variations of $\eta(\Phi = 0.11, T)$ inferred using the three laws are represented in figure 12 together with the measurements of Freysz (1990). This comparison calls for two remarks. (i) The relative differences between

the three laws are small, of order 10–15%. (ii) According to the difference between Einstein's and Batchelor's laws, a relevant quadratic correction to Taylor's law should increase the viscosity contrast between the two phases. Moreover, Danov (2001) claims that the behaviour of the viscosity of microemulsions is intermediate between solid suspensions and droplets not covered by surfactants. For these reasons, we believe that Einstein's law should reasonably describe the actual viscosity of a two-phase microemulsion. Finally, we stress that the flow should not critically depend on the viscosity contrast between both phases.

Appendix B. Electromagnetic stress exerted at an interface between two dielectrics: radiation pressure

The expression of the force balance at the interface (4.9) involves a contribution of the electromagnetic field called radiation pressure. In this appendix, we demonstrate that this interfacial stress of electromagnetic origin is actually normal to the interface and is expressed as (5.4).

Noting $\boldsymbol{E}_i$, $i=1,2$ the electric field in two dielectric media 1 and 2, we consider here only the part $\boldsymbol{T}_i'^{em}=\varepsilon_0\varepsilon_i\boldsymbol{E}_i\,{}^t\boldsymbol{E}_i-\varepsilon_0\varepsilon_i\boldsymbol{E}_i^2\boldsymbol{I}/2$, $i=1,2$ of the Maxwell stress tensor, the other part $(\varepsilon_0\rho/2)(\partial\varepsilon/\partial\rho)|_T\boldsymbol{E}^2\boldsymbol{I}$, called the electrostrictive term, that shows up through the pseudo-pressures $q_i=p_i-(\varepsilon_0\boldsymbol{E}_i^2\rho_i/2)(\partial\varepsilon_i/\partial\rho_i)|_T$, $i=1,2$ having no influence on the flow under study. Considering the interface between these two media, defining $\boldsymbol{n}_{1\to2}$ as the unit vector normal to the interface at point M of the interface and $(\boldsymbol{\alpha},\boldsymbol{\beta})$ as two orthogonal vectors lying in the plane tangent to the interface at point M, $(\boldsymbol{\alpha},\boldsymbol{\beta},\boldsymbol{n}_{1\to2})$ constitute an orthogonal base of unit vectors associated with M. Expressing the electric fields in this base as $\boldsymbol{E}_i=E_{\alpha,i}\boldsymbol{\alpha}+E_{\beta,i}\boldsymbol{\beta}+E_{n,i}\boldsymbol{n}_{1\to2}$ and noting $\boldsymbol{E}_{t,i}=E_{\alpha,i}\boldsymbol{\alpha}+E_{\beta,i}\boldsymbol{\beta}$, the components $(\Pi_{\alpha,i},\Pi_{\beta,i},\Pi_{n,i})$ of the force $\boldsymbol{\Pi}_i=(-1)^i\boldsymbol{T}_i'^{em}\boldsymbol{n}_{1\to2}$ exerted on the interface by medium i can be expressed as follows:

$$\Pi_{\alpha,i}=(-1)^i\boldsymbol{\alpha}\cdot\left[\boldsymbol{T}_i'^{em}\boldsymbol{n}_{1\to2}\right]=(-1)^i\varepsilon_0\varepsilon_iE_{\alpha,i}E_{n,i}=(-1)^iE_{\alpha,i}D_{n,i},\tag{B 1}$$

$$\Pi_{\beta,i}=(-1)^i\boldsymbol{\beta}\cdot\left[\boldsymbol{T}_i'^{em}\boldsymbol{n}_{1\to2}\right]=(-1)^i\varepsilon_0\varepsilon_iE_{\beta,i}E_{n,i}=(-1)^iE_{\beta,i}D_{n,i},\tag{B 2}$$

$$\Pi_{n,i}=(-1)^i\boldsymbol{n}_{1\to2}\cdot\left[\boldsymbol{T}_i'^{em}\boldsymbol{n}_{1\to2}\right]=\tfrac{1}{2}(-1)^i\varepsilon_0\varepsilon_i(E_{n,i}^2-E_{t,i}^2),\tag{B 3}$$

where $\boldsymbol{D}_i=\varepsilon_0\varepsilon_i\boldsymbol{E}_i$ is the electric displacement vector. Since Maxwell's equations imply that $D_{n,1}=D_{n,2}$ and $\boldsymbol{E}_{t,1}=\boldsymbol{E}_{t,2}$, the components along $\boldsymbol{\alpha}$ and $\boldsymbol{\beta}$ of the net force $\boldsymbol{\Pi}_1+\boldsymbol{\Pi}_2$ exerted on the interface are both zero. In contrast, its component along $\boldsymbol{n}_{1\to2}=\hat{\boldsymbol{r}}$ is

$$\Pi_{n,1}+\Pi_{n,2}=\tfrac{1}{2}\varepsilon_0\left((\varepsilon_1-\varepsilon_2)E_t^2-\varepsilon_1E_{n,1}^2+\varepsilon_2E_{n,2}^2\right).\tag{B 4}$$

Using $\varepsilon_i=n_i^2$ and the continuity of D_n across the interface, (B 4) becomes:

$$\Pi=\Pi_{n,1}+\Pi_{n,2}=\frac{1}{2}\varepsilon_0\left(n_1^2-n_2^2\right)\left(E_t^2+\frac{n_1^2}{n_2^2}E_{n,1}^2\right).\tag{B 5}$$

Once averaged over one period of oscillation of the monochromatic electric fields, it becomes (5.4).

REFERENCES

Ashkin, A. & Dziedzic, J. M. 1973 Radiation pressure on a free surface. *Phys. Rev. Lett.* **30**, 139–142.

Ashkin, A., Dziedzic, J. M. & Smith, P. W. 1982 Continuous-wave self-focusing and self-trapping of light in artificial Kerr media. *Opt. Lett.* **7** (6), 276–278.

Beysens, D., Bourgou, A. & Calmettes, P. 1982 Experimental determination of universal amplitude combinations for binary fluids. Part I. Statics. *Phys. Rev.* A **26**, 3589–2609.

Brasselet, E. & Delville, J. P. 2008 Liquid-core liquid-cladding optical fibers sustained by light radiation pressure: electromagnetic model and geometrical analog. *Phys. Rev.* A **78**, 013835.

Brasselet, E., Wunenburger, R. & Delville, J. P. 2008 Liquid optical fibers with a multistable core actuated by light radiation pressure. *Phys. Rev. Lett.* **101**, 014501.

Cametti, C., Codastefano, P., d'Arrigo, G., Tartaglia, P., Rouch, J. & Chen, S. H. 1990 Viscoelastic behavior of dense microemulsions. *Phys. Rev.* A **42**, 3421–3426.

Casner, A. & Delville, J.-P. 2001 Giant deformations of a liquid–liquid interface induced by the optical radiation pressure. *Phys. Rev. Lett.* **87**, 054503.

Casner, A. & Delville, J. P. 2003 Laser-induced hydrodynamic instability of fluid interfaces. *Phys. Rev. Lett.* **90**, 144503.

Casner, A. & Delville, J. P. 2004 Laser-sustained liquid bridges. *Europhys. Lett.* **65**, 337–343.

Casner, A., Delville, J. P. & Brevik, I. 2003 Asymmetric optical radiation pressure effects on liquid interfaces under intense illumination. *J. Opt. Soc. Am.* B **90**, 11.

Chraïbi, H., Lasseux, D., Arquis, E., Wunenburger, R. & Delville, J.-P. 2008*a* Simulation of an optically induced asymmetric deformation of a liquid–liquid interface. *Eur. J. Mech.* B/*Fluids* **27**, 419–432.

Chraïbi, H., Lasseux, D., Arquis, E., Wunenburger, R. & Delville, J.-P. 2008*b* Stretching and squeezing of sessile dielectric drops by the optical radiation pressure. *Phys. Rev.* E **77**, 066706.

Danov, K. D. 2001 On the viscosity of dilute emulsions. *J. Colloid Interface Sci.* **235** (1), 144–149.

Eggers, J. & Villermaux, E. 2008 Physics of liquid jets. *Rep. Prog. Phys.* **71**, 036601.

Freysz, E. 1990 Etude des non linéarités optiques dans les mélanges liquides binaires critiques. Thèse d'état, Université Bordeaux 1.

Freysz, E., Afifi, M. & Ducasse, A. 1985 Giant optical nonlinearities of critical microemulsions. *J. Phys. Lett.* **46**, L-181–L-187.

Freysz, E., Laffon, E., Delville, J. P. & Ducasse, A. 1994 Phase conjugation in critical microemulsions. *Phys. Rev.* E **49** (3), 2141–2149.

Gonzalez, H., McCluskey, F. M. J., Castellanos, A. & Barrero, A. 1989 Stabilization of dielectric liquid bridges by electric fields in the absence of gravity. *J. Fluid Mech.* **206**, 545–561.

Grigorova, B. M., Rastopov, S. F. & Sukhodol'skii, A. T. 1990 Coherent correlation spectroscopy of capillary waves. *Sov. Phys. Tech. Phys.* **35**, 374–376.

Harada, Y. & Asakura, T. 1996 Radiation forces on a dielectric sphere in the Rayleigh scattering regime. *Opt. Commun.* **124**, 529–541.

Hart, S. J. & Terray, A. V. 2003 Refractive-index-driven separation of colloidal polymer particles using optical chromatography. *Appl. Phys. Lett.* **83**, 5316–5218.

van de Hulst, H. C. 1957 *Light Scattering by Small Particles*. Dover.

Issenmann, B., Nicolas, A., Wunenburger, R., Manneville, S. & Delville, J. P. 2008 Deformation of acoustically transparent fluid interfaces by the acoustic radiation pressure. *Europhys. Lett.* **83**, 34002.

Jacobs, D. T. 1986 Turbidity in the binary fluid mixture methanol-cyclohexane. *Phys. Rev.* A **33**, 2605–2611.

Jean-Jean, B. 1987 Contributions thermique et électrostrictive aux non-linearités optiques géantes observées dans les microémulsions critiques. PhD thesis, Université Bordeaux 1.

Jean-Jean, B., Freysz, E., Ducasse, A. & Pouligny, B. 1988 Thermodiffusive and electrostrictive optical nonlinearities in critical microemulsions. *Europhys. Lett.* **7** (3), 219–224.

Jean-Jean, B., Freysz, E., Ponton, A., Ducasse, A. & Pouligny, B. 1989 Nonlinear propagation of Gaussian beams in binary critical liquid mixtures. *Phys. Rev.* A **39** (10), 5268–5279.

Johns, L. E. & Narayanan, R. 2002 *Interfacial Instability*. Springer.

Kaneta, T., Ishidzu, Y., Mishima, N. & Imasaka, T. 1997 Theory of optical chromatography. *Anal. Chem.* **69**, 2701–2709.

Kazaryan, M. A., Korotkov, N. P. & Zakharov, S. D. 1995 Hydrodynamic flows in suspensions caused by powerful pulse-periodic light beams. *Phys. Scr.* **52**, 678–679.

Kumar, A., Krishnamurty, H. R. & Gopal, E. S. R. 1983 Equilibrium critical phenomena in binary liquid mixtures. *Phys. Rep.* **98** (2), 57–143.

Kuznetsova, L. A. & Coakley, W. T. 2004 Microparticle concentration in short path length ultrasonic resonators: roles of radiation pressure and acoustic streaming. *J. Acoust. Soc. Am.* **116**, 1956–1966.

Landau, L., Lifshitz, E. & Pitayevski, L. 1984 *Electrodynamics of Continuous Media*, 2nd edn. Butterworth Heinemann.

Marr-Lyon, M. J., Thiessen, D. B. & Marston, P. L. 2001 Passive stabilization of capillary bridges in air with acoustic radiation pressure. *Phys. Rev. Lett.* pp. 2293–6.

McIntyre, M. E. 1981 On the 'wave-momentum' myth. *J. Fluid Mech.* **106**, 331–347.

Mitani, S. & Sakai, K. 2002 Measurement of ultralow with a laser interface manipulation technique. *Phys. Rev.* E **66**, 031604.

Mitani, S. & Sakai, K. 2005 Observation of interfacial tension minima in oil-water-surfactant systems with laser manipulation technique. *Faraday Discuss.* **129**, 141–153.

Moldover, M. R. 1985 Interfacial tension of fluids near critical points and two-scale-factor universality. *Phys. Rev.* A **31**, 1022–1033.

Monjushiro, H., Takeuchi, K. & Watarai, H. 2002 Anomalous laser photophoretic behavior of photo-absorbing organic droplets in water. *Chem. Lett.* pp. 788–789.

Nieto-Vesperinas, M., Chaumet, P. C. & Rahmani, A. 2009 Near-field photonic forces. *Phil. Trans. R. Soc. Lond.* A **362**, 719–737.

Nyborg, W. L. 1997 Acoustic streaming. In *Nonlinear Acoustics* (ed. M. F. Hamilton & D. T. Blackstock), pp. 207–232. Academic.

Ornstein, L. S. & Zernike, F. 1914 Accidental deviation of density and opalescence at the critical point of a single substance. *Proc. Kon. Ned. Akad. Wetensch.* **17**, 793–806.

Ostrovskaya, G. V. 1988*a* Deformation of the free surface of a liquid under the pressure of light. Part I. Theory. *Sov. Phys. Tech. Phys.* **33** (4), 465–468.

Ostrovskaya, G. V. 1988*b* Deformation of the free surface of a liquid under the pressure of light. Part II. Experiment. *Sov. Phys. Tech. Phys.* **33** (4), 468–470.

Padgett, M., Molloy, J. & McGloin, D. 2009 *Optical Tweezers: Methods and Applications*. CRC.

Pfeifer, R. N. C., Nieminen, T. A., Heckenberg, N. R. & Rubinsztein-Dunlop, H. 2007 Momentum of an electromagnetic wave in dielectric media. *Rev. Mod. Phys.* **79**, 1197–1216.

Puglielli, V. G. & Ford, N. C. 1970 Turbidity measurements in sf_6 near its critical point. *Phys. Rev. Lett.* **25** (3), 143–147.

Raco, R. J. 1968 Electrically supported column of liquid. *Science* **160**, 311–312.

Rohatscheck, H. 1985 Direction, magnitude and causes of photophoretic forces. *J. Aerosol. Sci.* **16**, 29–42.

Sakai, K., Mizumo, D. & Takagi, K. 2001 Measurement of liquid surface properties by laser-induced surface deformation spectroscopy. *Phys. Rev.* E **63**, 043602.

Sakai, K. & Yamamoto, Y. 2006 Electric field tweezers for characterization of liquid surface. *Appl. Phys. Lett.* **89**, 211911.

Savchenko, A. Yu., Tabiryan, N. V. & Zel'dovich, B. Ya. 1997 Transfer of momentum and torque from a light beam to a liquid. *Phys. Rev.* E **56**, 4773–4779.

Schäffer, E., Thrun-Albrecht, T., Russel, T. P. & Steiner, U. 2000 Electrically induced structure formation and pattern transfer. *Nature (London)* **403**, 874–877.

Schroll, R. D., Wunenburger, R., Casner, A., Zhang, W. W. & Delville, J.-P. 2007 Liquid transport due to light scattering. *Phys. Rev. Lett.* **98**, 133601.

Sengers, J. V. & Levelt-Sengers, J. M. H. 1978 Critical phenomena in classical fluids. In *Progress in Liquid Physics* (ed. C. A. Croxton), chap. 4, pp. 103–174. Wiley-Interscience.

Simpson, H. J. & Marston, P. L. 1995 Ultrasonic four-wave mixing mediated by an aqueous suspension of microspheres: theoretical steady-state properties. *J. Acoust. Soc. Am.* **98** (3), 1731–1741.

Smith, P. W., Maloney, P. J. & Ashkin, A. 1982 Turbidity measurements in sf_6 near its critical point. *Opt. Lett.* **7** (8), 147–149.

Snyder, A. W. & Love, J. D. 1983 *Optical Waveguide Theory*. Kluwer Academic.

Tan, M. K., Friend, J. R. & Yeo, L. Y. 2009 Interfacial jetting phenomenon induced by focused surface vibrations. *Phys. Rev. Lett.* **103**, 024501.

Thouvenel-Romans, S., van Saarloos, W. & Steinbock, O. 2004 Silica tubes in chemical gardens: radius selection and its hydrodynamic origin. *Europhys. Lett.* pp. 42–48.

Weast, R. C., (ed.) 1971 *Handbook of Chemistry and Physics*, 52nd edn. The Chemical Rubber Co.

Wohluter, F. K. & Basaran, O. A. 1992 Shapes and stability of pendant and sessile dielectric drops in an electric field. *J. Fluid Mech.* **235**, 481–510.

Wood, R. W. & Loomis, A. L. 1927 The physical and biological effects of high-frequency sound waves of great intensity. *Phil. Mag.* **4**, 417.

Wunenburger, R., Casner, A. & Delville, J.-P. 2006*a* Light-induced deformation and instability of a liquid interface. Part I. Statics. *Phys. Rev.* E **73**, 036314.

Wunenburger, R., Casner, A. & Delville, J.-P. 2006*b* Light-induced deformation and instability of a liquid interface. Part II. Dynamics. *Phys. Rev.* E **73**, 036315.

Yoshitake, Y., Mitani, S., Sakai, K. & Takagi, K. 2005 Measurement of high viscosity with laser induced surface deformation technique. *J. Appl. Phys.* **97**, 024901.

Yoshitake, Y., Mitani, S., Sakai, K. & Takagi, K. 2008 Surface tension and elasticity of gel studied with laser-induced surface-deformation spectroscopy. *Phys. Rev.* E **78**, 041405.

Zakharov, S. D., Kazaryan, M. A. & Korotkov, N. P. 1994 Shock acceleration of particles in a laser beam. *JETP Lett.* **60**, 322–324.

Zeleny, J. 1914 The electrical discharge from liquid points, and a hydrostatic method of measuring the electric intensity at their surfaces. *Phys. Rev.* **3**, 69–91.

Zhang, J. Z. & Chang, R. K. 1988 Shape distortion of a single water droplet by laser-induced electrostriction. *Opt. Lett.* **13**, 916–918.